NEUROSCIENCE

Beta2 adrenergic receptor–mediated abnormal myelopoiesis drives neuroinflammation in aged patients with traumatic brain injury

Rui Jiang[1,2]†, Zhichao Lu[1,2]†, Chenxing Wang[1,2]†, Jun Xiao[1,3], Qianqian Liu[1,4], Xide Xu[1,4], Jinlong Shi[1,4], Jianhong Shen[1,4], Xingjia Zhu[1,4], Peipei Gong[1,4], Qian-Xing Zhuang[5]*, Kaibin Shi[2,6]*, Wei Shi[1,4]*

Aged patients often suffer poorer neurological recovery than younger patients after traumatic brain injury (TBI), but the mechanisms underlying this difference remain unclear. Here, we demonstrate abnormal myelopoiesis characterized by increased neutrophil and classical monocyte output but impaired nonclassical patrolling monocyte population in aged patients with TBI as well as in an aged murine TBI model. Retrograde and anterograde nerve tracing indicated that increased adrenergic input through the central amygdaloid nucleus–bone marrow axis drives abnormal myelopoiesis after TBI in a β2-adrenergic receptor–dependent manner, which is notably enhanced in aged mice after injury. Selective blockade of β2-adrenergic receptors rebalances abnormal myelopoiesis and improves the outcomes of aged mice after TBI. We therefore demonstrate that increased β2-adrenergic input-driven abnormal myelopoiesis exacerbates post-TBI neuroinflammation in the aged, representing a mechanism underlying the poorer recovery of aged patients and that blockade of β2-adrenergic receptor is a potential approach to promote neurological recovery after TBI.

INTRODUCTION

Traumatic brain injury (TBI) is a leading cause of death and disability worldwide (*1*, *2*). Besides craniotomy, a life-saving measure for severe patients, there is currently no approved pharmacologic treatment for TBI (*3*). The incidence of TBI in the aged population has risen rapidly over the past decades; patients older than 65 years have the highest frequency of hospital admissions caused by TBI and a twice of the mortality of young patients (*4*–*6*). Growing evidence suggests that an imbalance in the immune response may be responsible for the higher mortality, greater susceptibility to secondary infections, and poorer behavioral recovery (*7*–*9*). Aging has profound effects on the immune system, manifested as myeloid-biased hematopoiesis and changes in lymphocyte phenotypes, but the extent to which these age-related changes affect the outcome of TBI is still unclear.

Acute brain injury rapidly orchestrates the peripheral immune system (*10*). Triggering leukocyte infiltration of the brain parenchyma, myeloid cells including neutrophils and monocytes reach the brain within hours of injury and peak in number several days after the initial injury, outnumbering other immune cell subtypes (*11*). How aging affects the composition and function of myeloid cell subpopulations infiltrating the brain parenchyma after TBI is still unclear. Bone marrow is involved in the continued supply of myeloid cells to the brain after TBI (*12*). Aged bone marrow is characterized by exacerbated myelopoiesis. We therefore examined the cranial bone marrow of patients who underwent debridement surgery to clarify the effects of aging on hematopoietic and immune systems of patients with TBI. We uncover that aged patients with TBI exhibit abnormal myelopoiesis characterized by increased neutrophil, classical monocyte output, and impaired nonclassical monocyte production. Increased adrenergic input from the central amygdaloid nucleus (CeA)–bone marrow axis drives abnormal post-TBI myelopoiesis in a β2-adrenergic receptor–dependent manner, which is notably enhanced in aged mice after injury. Selective blockade of β2-adrenergic receptors rebalances abnormal myelopoiesis and improves prognosis in aged mice after TBI.

RESULTS

Aging drives bone marrow HSCs toward the myeloid lineage and inhibits the differentiation of nonclassical monocytes in patients with TBI

We initially characterized the composition of the major myeloid and lymphoid cells in the peripheral blood of patients with TBI, including neutrophils ($CD45^+CD15^+CD16^+CD66b^+$), nonclassical monocytes ($CD45^+CD14^+CD16^+$), classical monocytes ($CD45^+CD14^+CD16^-$), T cells ($CD45^+CD3^+$), and B cells ($CD45^+CD3^-CD19^+$). Compared to healthy individuals, patients with TBI had significantly more myeloid cells in peripheral blood, whereas they had significantly fewer lymphocytes in the peripheral blood after TBI. Neutrophil counts in the peripheral blood of patients with TBI peaked as early as day 1 after TBI, and monocyte counts peaked on day 3 after TBI. The numbers of neutrophils and classical monocytes in the peripheral blood of aged patients with TBI were significantly higher than those in the peripheral blood of young patients with TBI. In contrast, the number of nonclassical monocytes in the peripheral blood of young patients with TBI was consistently greater than that in the peripheral blood of aged

[1]Department of Neurosurgery, Research Center of Clinical Medicine, Affiliated Hospital of Nantong University, Medical School of Nantong University, Nantong, Jiangsu 226001, China. [2]Department of Neurology, China National Clinical Research Center for Neurological Diseases, Beijing Tiantan Hospital, Capital Medical University, Beijing 100070, China. [3]Key Laboratory of RNA Science and Engineering, CAS Center for Excellence in Molecular Cell Science, Shanghai Institute of Biochemistry and Cell Biology, University of Chinese Academy of Sciences, Chinese Academy of Sciences, Shanghai 200031, China. [4]Neuro-Microscopy and Minimally Invasive Translational Medicine Innovation Center, Affiliated Hospital of Nantong University, Nantong, Jiangsu 226001, China. [5]Department of Physiology, School of Medicine, Nantong University, Nantong, Jiangsu 226001, China. [6]Chinese Institutes for Medical Research, Beijing 100069, China.
*Corresponding author. Email: qxzhuang@ntu.edu.cn (Q.-X.Z.); kshi@cimrbj.ac.cn (K.S.); fysw@ntu.edu.cn (W.S.)
†These authors contributed equally to this work.

patients (Fig. 1A and fig. S1A). The serum levels of the anti-inflammatory cytokines interleukin-4 (IL-4) and IL-10 were higher in young patients, while the levels of proinflammatory cytokines, including tumor necrosis factor–α (TNF-α) and IL-1β, were lower in young patients (fig. S2, A to D).

To better understand whether the differences in peripheral immune profiles between young and aged patients affect the inflammatory milieu of the injured brain, we collected brain tissue removed from patients who underwent surgery and investigated the numbers of immune cells infiltrating the brain. Consistent with the changes in the peripheral immune system, there was a surge of infiltrating neutrophils and monocytes during the acute phase of injury, with neutrophils peaking on day 1 and monocytes continuously increasing to day 7 after injury. Regarding age-dependent differences, the frequencies of infiltrating neutrophils and classical monocytes in the brain were significantly higher in aged patients with TBI than in young patients with TBI, while the frequency of nonclassical monocytes was higher in the brains of young patients than in those of aged, consistent with the findings on day 7 (Fig. 1B and fig. S3A). The frequency of lymphocytes in the central nervous system (CNS) increases continuously after TBI and is comparable between young and aged individuals. These data demonstrate a discrepancy in myeloid responses between young and aged patients with TBI, which might contribute to the different disease outcomes.

Myeloid cells have relatively short longevity, and the replenishment of cells from hematopoietic organs [e.g., bone marrow–derived hematopoietic stem cells (HSCs) and progenitor cells] is often enhanced during acute injuries and infections (*12*–*14*). To assess the response of the hematopoietic system in young and aged patients after TBI, we obtained bone marrow cells from skull bone flaps removed from patients with TBI who underwent decompression surgery. After TBI, we observed a significant increase in the proportion of HSCs in the cranial bone marrow of aged patients with TBI compared to young patients, which was accompanied by an increase in the proportion of $Ki67^+$ HSCs (Fig. 1, C to E), suggesting enhanced proliferation ability. To characterize the fate of HSCs in the cranial bone marrow after TBI, we detected downstream changes in the proportion of progenitor cells. Flow cytometry suggested a significant increase in the proportion of myeloid progenitors, including common myeloid progenitors (CMPs) and granulocyte-monocyte progenitors (GMPs), in the cranial bone marrow of aged patients with TBI. In contrast, the proportion of common lymphoid progenitor cells (CLPs) decreased (Fig. 1F). These results suggest that TBI increases the activity of HSCs in the bone marrow of patients and skews hematopoiesis toward myeloid hematopoiesis, which is more prominent in aged patients with defective nonclassical monocyte population (Fig. 1G).

Aging drives bone marrow HSCs toward the myeloid lineage and inhibits the differentiation of Ly6C^{low} monocytes in TBI mice

To further clarify the mechanisms underlying the discrepancy in myelopoiesis between young and aged patients with TBI, we created a controlled cortical impact (CCI) TBI murine model. Evaluation of neurological function showed that young mice had a faster and better recovery in sensorimotor function than did aged mice after TBI (fig. S4, H to I). Consistent with our findings in patients with TBI, the number and proportion of HSCs and progenitor cells ($Lineage^-$c-Kit^+Sca1^+), termed as LSKs, were significantly increased in the bone marrow of mice after TBI, and aged TBI mice showed more intense LSKs expansion than young mice. We then tested whether the increased LSKs in bone marrow were motivated to the blood and exert extramedullary hematopoiesis and found that the number and proportion of LSKs in peripheral blood and spleen significantly decreased after TBI in both young and aged mice (fig. S5, A to F), in agreement with a previous study (*15*). In addition, we similarly found a significant increase in the number of CMPs, GMPs, and monocyte-dendritic progenitors (MDPs) as well as a significant decrease in the number of CLPs in the bone marrow of TBI mice compared to sham controls, while the responses were more prominent in aged mice than in young mice after TBI (Fig. 2, A to F, and figs. S4A and S6, A to H).

We next evaluated whether the changes in progenitor cells gave rise to mature myeloid cells in the bone marrow of aged and young TBI mice (Fig. 2G). The results of flow cytometry showed that the numbers of neutrophils and Ly6C^{high} monocytes (corresponding to classical monocytes in humans) were significantly increased in the bone marrow of TBI mice. Notably, compared to those in young TBI mice, the numbers of neutrophils and Ly6C^{high} monocytes were higher in the bone marrow of aged TBI mice, whereas the number of Ly6C^{low} monocytes (corresponding to nonclassical monocytes in humans) was relatively lower in aged mice (Fig. 2H), suggesting a defected Ly6C^{low} monocytes population in aged mice after TBI. We then longitudinally observed changes in monocyte subtypes from surgery to 28 days after TBI. The number of Ly6C^{low} monocytes in the bone marrow of young TBI mice increased rapidly after injury and was significantly higher than Ly6C^{low} monocytes count of bone marrow of aged TBI mice from day 1 to 7 after TBI. In contrast, the number of Ly6C^{high} monocytes in the bone marrow of aged TBI mice was consistently higher than that in the bone marrow of young mice until day 28 after TBI (Fig. 2, I and J). Regarding the relative proportions of monocyte subtypes in each group, the frequency of Ly6C^{low} monocytes in the bone marrow of young mice rose rapidly after TBI, outnumbering Ly6C^{high} monocytes on day 1, whereas the frequency of Ly6C^{low} monocytes in the bone marrow of aged TBI mice rose at a slower rate, outnumbering Ly6C^{high} monocytes till day 7 (Fig. 2, K and L). To further figure out the fate of increased bone marrow LSKs, we performed lineage tracing of bone marrow HSC differentiation by adopting Fgd5-CreER-tdTomato mouse line, in which, HSCs and their downstream progenitors and mature cells will be labeled by tdTomato upon activation by tamoxifen (*10*, *16*). Compared to sham control, TBI significantly increased the proportion of tdTomato$^+$ HSCs and myeloid progenitors in the bone marrow of Fgd5-CreER-tdTomato mice, confirming the increased myelopoiesis in the bone marrow after TBI. In addition, tdTomato$^+$ Ly6C^{low} monocytes were significantly increased in the bone marrow of young Fgd5-CreER-tdTomato mice, but not Ly6C^{high} monocytes, suggesting enhanced Ly6C^{low} monocyte generation in young mice after TBI (fig. S7, A and B). Moreover, the serum concentrations of TNF-α and IL-1β were higher in aged TBI mice, and the serum concentrations of IL-4 and IL-10 were higher in young TBI mice after TBI (fig. S4, B to E).

To further clarify whether changes in the hematopoietic system affect the development of neuroinflammation after TBI, we examined the number of myeloid cells infiltrating the brain after TBI. We detected more neutrophils and Ly6C^{high} monocytes in the brains of aged mice, but there were more Ly6C^{low} monocytes in the brains of young mice after TBI (Fig. 2, M and N). The proportions of monocytes that produce cytokines including IL-1β, IL-6, and TNF-α were higher in aged brains than in young brains after TBI, while IL-10$^+$ monocytes were more abundant in young brains (Fig. 2O and fig. S8A). Immunofluorescence suggested that brain-infiltrating macrophages in young

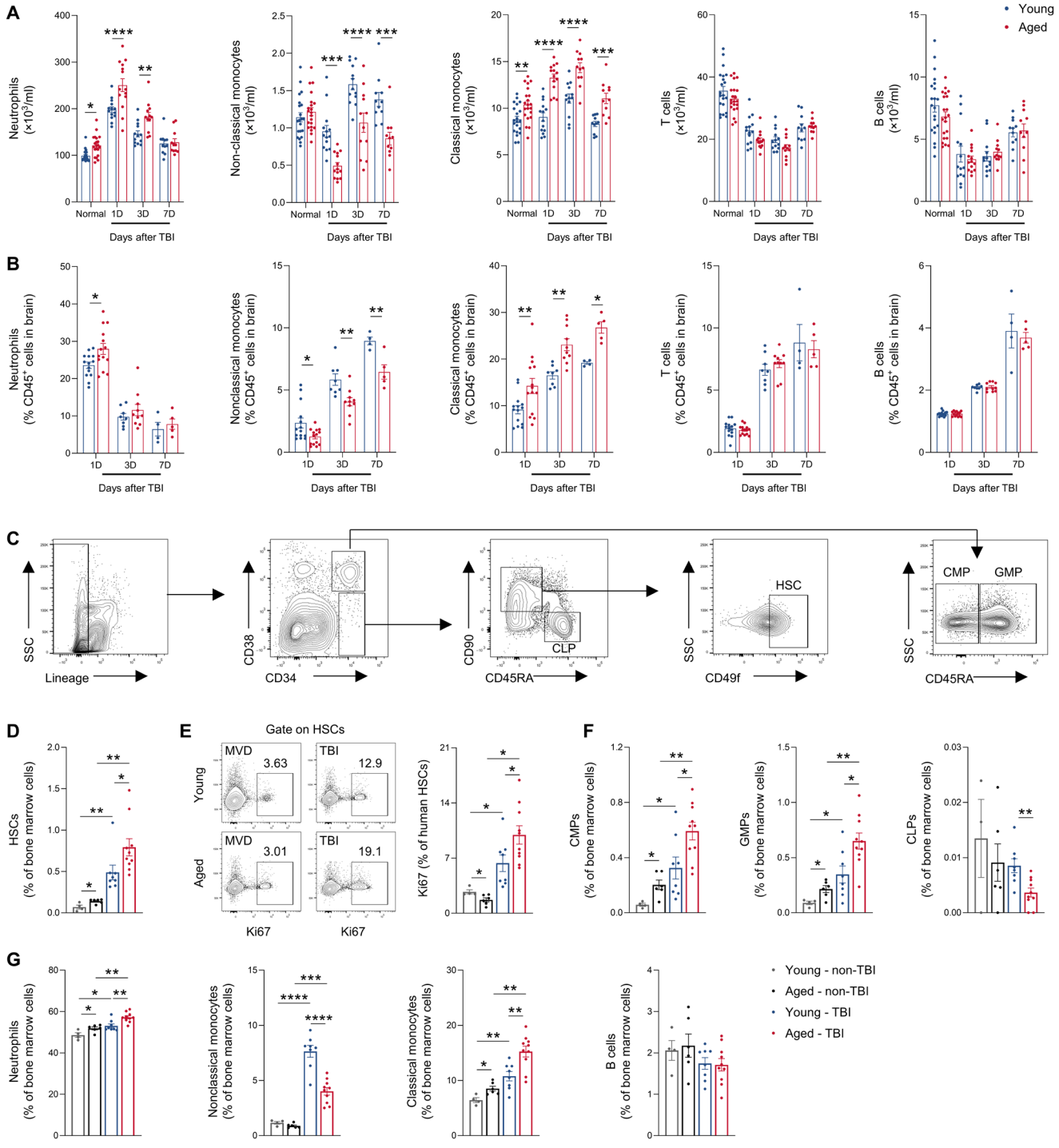

Fig. 1. Aging drives bone marrow HSCs toward myeloid lineage and inhibits nonclassical monocyte response in patients with TBI. (**A**) Bar plots show the numbers of neutrophils, nonclassical monocytes, classical monocytes, T cells, and B cells in the peripheral blood. $n = 21$ in normal young or aged; $n = 14, 14, 11$ in young patients with TBI at days 1, 3, and 7; $n = 14, 12, 11$ in aged patients with TBI at days 1, 3, and 7. (**B**) Bar plots show the proportions of neutrophils, nonclassical monocytes, classical monocytes, T cells, and B cells in brain tissue of patients with TBI. $n = 14, 8, 4$ in young patients with TBI at days 1, 3, and 7; $n = 14, 10, 5$ in aged patients with TBI at days 1, 3, and 7. (**C**) Flow cytometry gating strategy for human bone marrow cell lineages, including HSCs ($Lin^-CD38^-CD34^+CD90^+CD45RA^-CD49f^+$), CMPs ($Lin^-CD38^+CD34^+CD45RA^-$), GMPs ($Lin^-CD38^+CD34^+CD45RA^+$), and CLPs ($Lin^-CD38^-CD34^+CD90^-CD45RA^+$). (**D**) Graph shows the percentage of HSCs in cranial bone marrow. (**E**) Flow cytometry plots and bar plots show $Ki67^+$ HSCs in cranial bone marrow. (**F**) Bar plots show the percentages of CMPs, GMPs, and CLPs in cranial bone marrow. (**G**) Bar plots show the frequencies of neutrophils, nonclassical monocytes, classical monocytes, and B cells in cranial bone marrow. (D to G) Young non-TBI, $n = 4$; aged non-TBI, $n = 6$; young TBI, $n = 8$; aged TBI, $n = 10$. Data are represented as means ± SEM. $^*P < 0.05$, $^{**}P < 0.01$, $^{***}P < 0.001$, $^{****}P < 0.0001$. Statistical analyses were performed using two-tailed unpaired Student's *t* test (D to G) and two-way analysis of variance (ANOVA) followed by Tukey post hoc test (A and B).

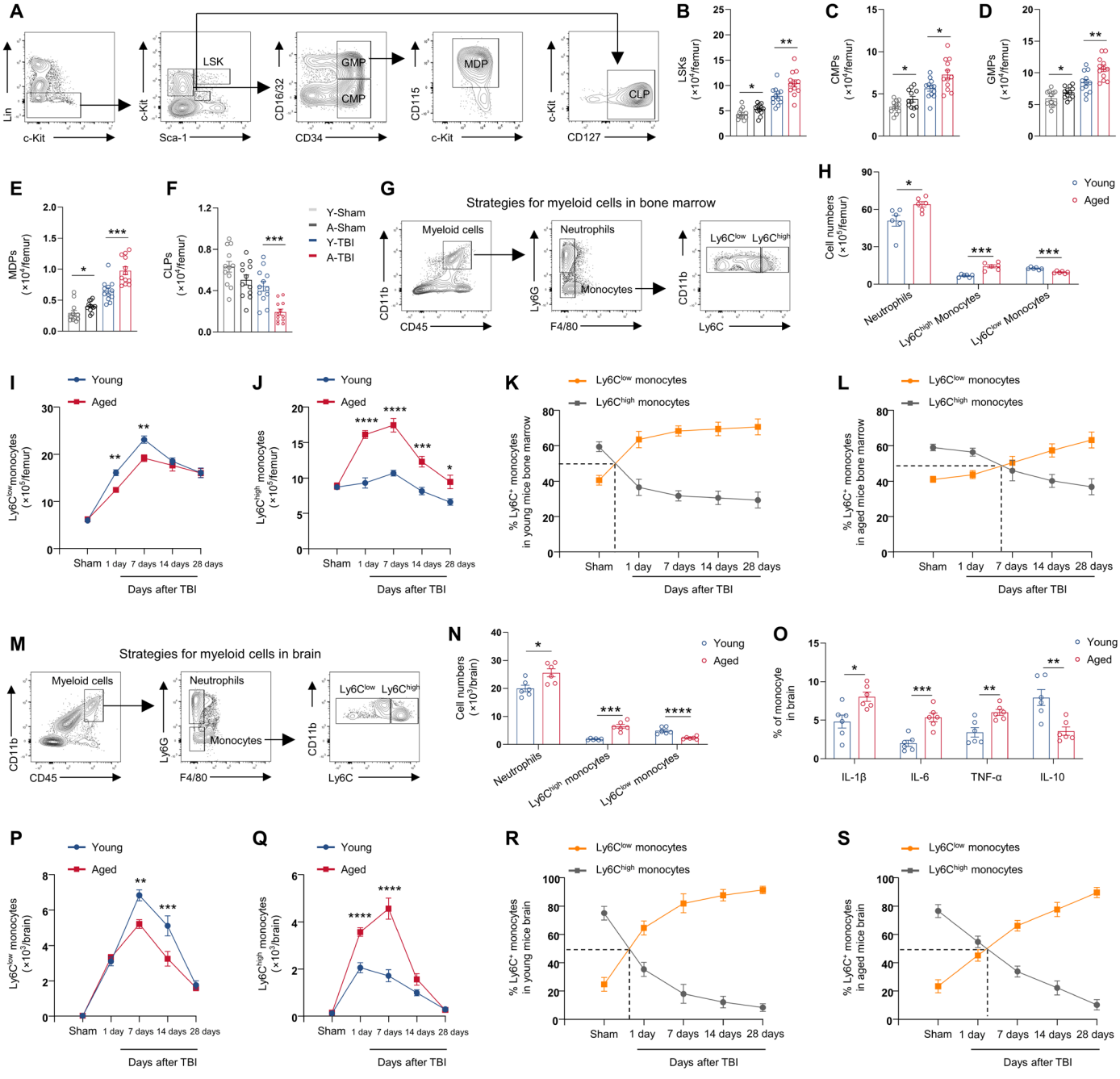

Fig. 2. Aging drives bone marrow HSCs toward myeloid lineage and inhibits Ly6C^{low} monocyte response in TBI mice. (**A**) Flow cytometry gating strategy for mouse bone marrow cell lineages, including LSK (Lin$^-$Sca-1$^+$c-Kit$^+$), CMP (Lin$^-$Sca-1$^-$c-Kit$^+$CD34$^+$CD16/32^{int}), GMP (Lin$^-$Sca-1$^-$c-Kit$^+$CD34$^+$CD16/32^{hi}), MDP (Lin$^-$Sca-1$^-$c-Kit$^+$CD34$^+$CD16/32^{hi}CD115$^+$), and CLP (Lin$^-$Sca-1^{int}c-Kit^{int}CD127$^+$). (**B** to **F**) Bar plots show counts of LSKs, CMPs, GMPs, MDPs, and CLPs in bone marrow of young and aged mice at day 3 after TBI. (**G**) Flow cytometry gating strategies for myeloid cells in mouse bone marrow, including neutrophils (CD45$^+$CD11b$^+$F4/80$^-$Ly6G$^+$), Ly6C^{low} monocytes (CD45$^+$CD11b$^+$F4/80$^-$Ly6G$^-$Ly6C^{low}), and Ly6C^{high} monocytes (CD45$^+$CD11b$^+$F4/80$^-$Ly6G$^-$Ly6C^{high}). (**H**) Bar plot shows the numbers of neutrophils and monocytes in bone marrow at day 3 after TBI. (**I** and **J**) Changes of bone marrow Ly6C^{low} and Ly6C^{high} monocyte counts after TBI. (**K** and **L**) Changes of Ly6C^{low} and Ly6C^{high} monocytes proportion in total monocytes in young and aged bone marrow. (**M** and **N**) Flow cytometry gating strategies of bone marrow myeloid cells. Bar plot shows the numbers of neutrophils, Ly6C^{low}, and Ly6C^{high} monocytes in the brains on day 3 after TBI. (**O**) Bar plot shows the proportions of IL-1β$^+$, IL-6$^+$, TNF-α$^+$, and IL-10$^+$ monocytes at day 3 after TBI. (**P** and **Q**) Line plots show changes in the number of Ly6C^{low} and Ly6C^{high} monocytes in the bone marrow. (**R** and **S**) Line plots show changes in the proportions of Ly6C^{low} and Ly6C^{high} monocytes in total monocytes in the brains. n = 12 per group for (B) to (F). n = 6 per group for (H) to (L) and (N) to (S). Data are represented as means ± SEM. *P < 0.05, **P < 0.01, ***P < 0.001, ****P < 0.0001. Statistical analyses were performed using two-tailed unpaired Student's t test (B to F, H, N, and O) and two-way ANOVA followed by Tukey post hoc test (I and J and P and Q).

TBI mice highly expressed CD206, programmed cell death ligand 1 (PD-L1), and IL-10 compared with those in aged TBI mice (fig. S4, F and G). Consistent with the changes in the bone marrow after TBI, the number of brain-infiltrated Ly6C^{low} monocytes in young mice rose rapidly after TBI to a significantly higher proportion than that in aged mice at 7 and 14 days after TBI (Fig. 2, P and Q). In contrast, Ly6C^{high} monocytes predominated in the brains of aged TBI mice, recapitulating the findings in patients with TBI. Similarly, the proportion of Ly6C^{low} monocytes in the brains of young mice rose rapidly after injury, with a proportional reversal occurring before day 1, whereas the proportion of Ly6C^{low} monocytes in the brains of aged TBI mice rose at a slower rate, the proportional reversal occurring after day 1 (Fig. 2, R and S). These data demonstrate that bone marrow population of Ly6C^{low} monocytes is impaired in aged subjects, which potentially contribute to their overwhelming brain inflammation and poorer outcomes.

Increased adrenergic input through the CeA–bone marrow axis drives abnormal myelopoiesis after TBI

Hematopoiesis is coordinately regulated by short-range focal signals as well as long-range signals (*17*). Sympathetic nervous system (SNS) is involved in hematopoiesis regulation (*18*). To test whether SNS contributes to the abnormal myelopoiesis after TBI, we measured the serum norepinephrine (NE) concentration in young and aged patients with TBI and in healthy controls. In healthy controls, serum NE in aged adults were higher than that in young adults. TBI induced a significant increase of seral NE concentration in both young and aged patients. Serum NE was significantly higher in aged than in young patients with TBI (Fig. 3A). Tyrosine hydroxylase (TH) staining of skulls obtained postoperatively from patients with TBI showed a higher density of sympathetic nerves in the skulls of aged patients with TBI, consistent with the elevated NE concentration in the supernatant of aged patients (Fig. 3, B to D).

To localize the brain region that innervates bone marrow, we retrogradely traced the nervous system by injecting red fluorescent protein–labeled pseudorabies virus (PRV-RFP) into the femur bone marrow of mice. Three days after virus injection, we observed red fluorescent signals in the paraventricular nucleus (PVN), CeA, and zona incerta (ZI) regions (Fig. 3E). To further confirm which region directly affects the bone marrow, we subsequently injected an adeno-associated virus overexpressing jRGECO1a (AAV9-jRGECO1a) in the above three regions and combined it with a fiber-optic recording system to record calcium imaging signal (Fig. 3F). Calcium imaging signals in the CeA showed strong enhancement after TBI that persisted until day 7 after injury (Fig. 3, G and H), while the signals remained unchanged in the PVN and ZI (Fig. 3, I and J). In addition, anterograde nerve tracing by injecting herpes simplex virus (HSV) labeled with green fluorescent protein (GFP) with TH as a promoter (HSV-TH-GFP) in the CeA region showed that the CeA directly innervates the bone marrow (fig. S9). Correspondingly, NE significantly increased in peripheral blood and bone marrow supernatant after TBI, and it was even higher in aged mice than in young mice (Fig. 3, K and L), as was the number of TH$^+$ fibers in bone marrow (Fig. 3M). These results are in agreement with the results observed in human patients with TBI.

We then tested whether the activity of CeA neurons was responsible for bone marrow myelopoiesis. We used a chemical genetics approach with muscarinic receptor–based DREADD to manipulate the activity of TH$^+$ neurons in the CeA. Gq-coupled DREADD (hM3Dq) was used to enhance neuronal activity, while Gi/o-coupled DREADD (hM4Di) was used to inhibit neuronal activity. After 30 days of AAV9-TH-hM4Di or AAV9-TH-hM3Dq virus injection into the CeA of the brains of young and aged mice, the mice were treated with deschloroclozapine (DCZ) for 7 days to modulate electrophysiological activity in the CeA after TBI was induced. Electrophysiological recordings revealed that CeA neuronal activity was inhibited in mice receiving AAV9-TH-hM4Di injection and up-regulated in mice receiving AAV9-TH-hM3Dq injection (Fig. 4A and fig. S10, A to D). Under physiological conditions, the inhibition of CeA by AAV9-TH-hM4Di resulted in the suppression of bone marrow hematopoiesis throughout the lineage, whereas the enhancement of CeA by hM3Dq resulted in the enhancement of bone marrow hematopoiesis (fig. S11, A to J). However, the TBI-induced hematopoietic progenitor cell response and myelopoiesis of neutrophils and Ly6C^{high} monocytes were inhibited in the hM4Di group and enhanced in the hM3Dq group, while the changes in Ly6C^{low} monocytes were the opposite (Fig. 4, B to I). Correspondingly, the number of neutrophils and Ly6C^{high} monocytes infiltrating the brain decreased in the hM4Di group and increased in the hM3Dq group, whereas the number of brain-infiltrating Ly6C^{low} monocytes increased in the hM4Di group but decreased in the hM3Dq group (Fig. 4, J to L). CD86 was down-regulated in monocyte-derived macrophages in the TBI brain, but CD206 and PD-L1 were up-regulated in the hM4Di group after TBI (Fig. 4, M to P). We then evaluated whether the modulation of CeA activity could affect the outcome of TBI mice. Both young and aged hM4Di mice showed better neurological recovery and smaller lesion sizes after TBI, whereas neurological damage and lesion size were exacerbated in the hM3Dq group (Fig. 4, Q to S). Together, these findings indicate that TBI increases adrenergic input via the CeA–bone marrow axis, which promotes neutrophil and Ly6C^{high} monocyte generation with impaired Ly6C^{low} monocyte response, exacerbating neuroinflammation and worsening outcomes of TBI mice.

Adrenergic β2 receptor signaling mediates impaired Ly6C^{low} monocyte response in aged TBI mice

To further uncover the mechanism underlying impaired Ly6C^{low} monocyte response in aged TBI mice, we tested whether aged bone marrow progenitor cells are responsible for abnormal myelopoiesis by transplanting bone marrow cells from aged GFP mice to 8-month-old mice. Mice that received transplantation of young bone marrow were used as controls. Compared with young bone marrow–transplanted mice, aged bone marrow–transplanted mice showed higher CMPs, GMPs, and MDPs in the bone marrow, together with higher neutrophil and Ly6C^{high} monocyte output. However, the population of Ly6C^{low} monocytes was insufficient in aged bone marrow–transplanted mice (Fig. 5, A to C). Moreover, the brains of TBI mice that received aged bone marrow transplants exhibited greater infiltration of neutrophils and Ly6C^{high} monocytes, while they had fewer Ly6C^{low} monocytes (Fig. 5, D and E, and fig. S12, A and B). These data recapitulate bone marrow responses in aged versus young mice after TBI, suggesting that aged bone marrow progenitor cells are involved in abnormal myelopoiesis after TBI.

We then performed RNA sequencing of the bone marrow to study the molecular mechanisms underlying the discrepant bone marrow responses between aged and young mice before and after TBI. We isolated bone marrow from mice femurs on day 3 after TBI. The results of principal components analysis (PCA) showed that the transcriptomes of bone marrow samples from aged and young mice before and after TBI were spatially separated, suggesting distinct transcriptional

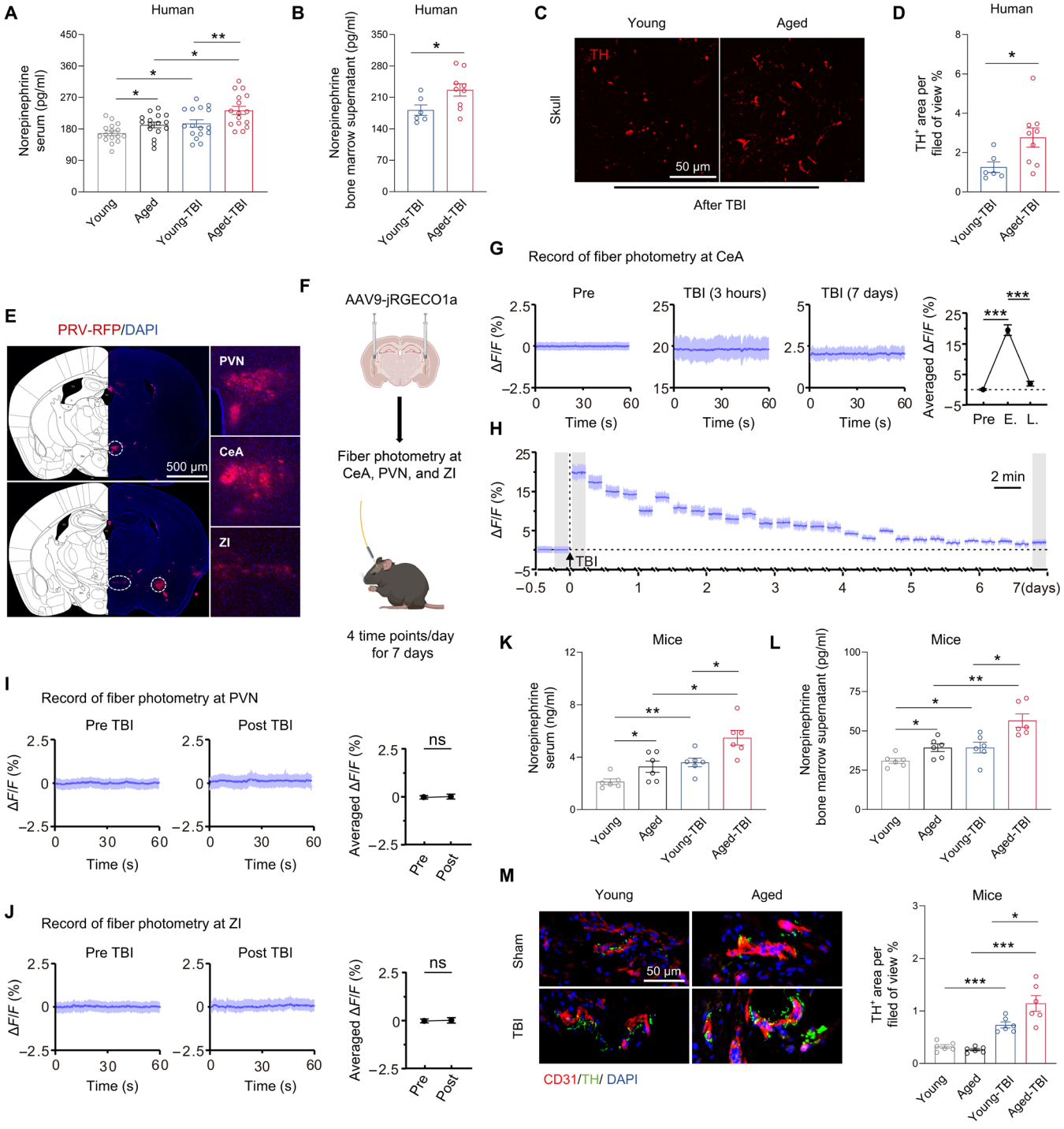

Fig. 3. CeA innervates bone marrow through SNS. (**A**) Bar plot shows NE concentrations in the peripheral blood of aged and young patients with TBI. (**B**) Bar plot shows NE concentrations in cranial bone marrow supernatants after TBI. (**C**) Images show sympathetic nerve fibers in surgically removed cranial bone flaps of patients with TBI; scale bar is shown in the figure. (**D**) Bar plot shows the percentage of TH^+ sympathetic fibers. (**E**) Images show brain labeled with red fluorescence after bone marrow injection of pseudorabies virus with a red fluorescent reporter gene in mice; scale bar is shown in the figure. (**F**) Experimental schematic of calcium imaging (created with BioRender.com). (**G**) The mean fluorescence signals within the CeA were measured at 3 hours before (pre), 3 hours after (early), and 7 days after TBI (late), respectively. (**H**) The mean fluorescence signals were measured from 0.5 days before to 7 days after TBI. (**I** and **J**) The mean fluorescence signals within the PVN and ZI were measured 3 hours before (Pre) and after TBI (Post). (**K**) Bar plot shows NE concentrations in the peripheral blood before and after TBI. (**L**) Bar plot shows NE concentrations in femur bone marrow supernatants before and after TBI. (**M**) Images and quantitative analysis of bone marrow TH expression before and after TBI; scale bar is shown in the figure. $n = 16$ per group for (A). $n = 6$ to group for (B), (D), and (M). $n = 9$ per group for (G), (I), and (J). Data are represented as means ± SEM. $^*P < 0.05$, $^{**}P < 0.01$, $^{***}P < 0.001$. Statistical analyses were performed using two-tailed unpaired Student's *t* test (A and B, D, I and J, and K to M) and one-way ANOVA followed by Tukey's post hoc test (G). ns., not significant.

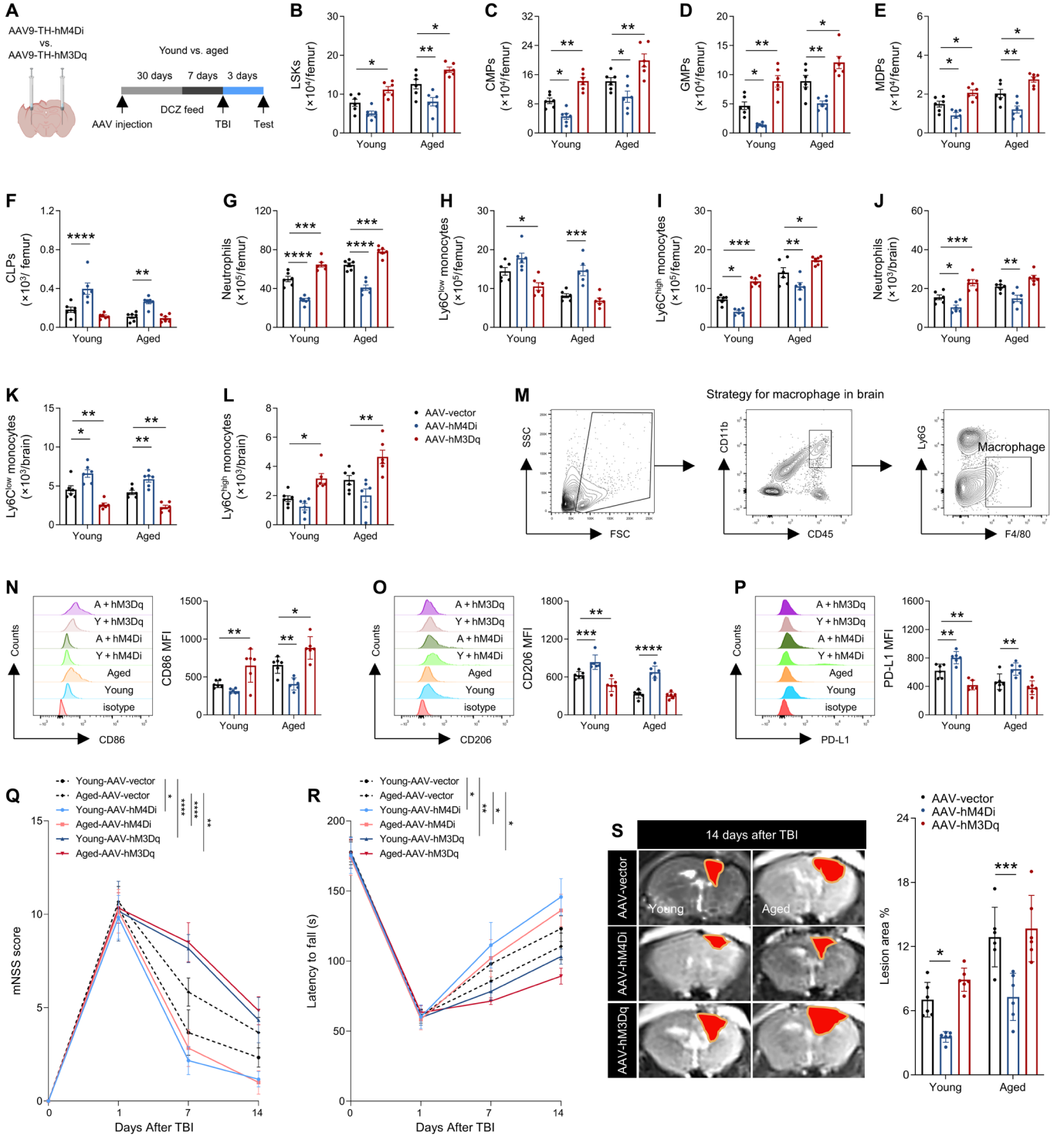

Fig. 4. CeA activity shapes bone marrow hematopoiesis and neuroinflammation after TBI. (**A**) Flow chart shows experiment design: aged and young mice received intraparenchymal injection of AAV9-TH-hM4Di and AAV9-TH-hM3Dq viruses in CeA; 30 days later, mice were fed with DCZ to modulate the neurophysiological activity of CeA neurons. Samples were taken on day 3 after TBI for flow cytometry (created with BioRender.com). (**B** to **I**) Bar plots show the numbers of LSKs, CMPs, GMPs, MDPs, CLPs, neutrophils, Ly6C^{low} monocytes, and Ly6C^{high} monocytes in femoral bone marrow of aged and young TBI mice. (**J** to **L**) Bar plots show the numbers of neutrophils, Ly6C^{low} monocytes, and Ly6C^{high} monocytes in the brains of aged and young TBI mice. (**M**) Flow cytometry plots show the gating strategies of macrophages (CD45^{+}CD11b^{+}Ly6G^{-}F4/80^{+}) in the brain. (**N** to **P**) Flow cytometry histograms and bar plots show the phenotype of macrophages in the brains of aged and young TBI. (**Q**) Modified neurological severity score (mNSS) of aged and young TBI mice in indicated groups. (**R**) Latency to fall in rotarod test for aged and young TBI mice in indicated groups. (**S**) MRI images and counts of brain lesions in aged and young TBI mice in indicated groups. n = 6 per group. Data are represented as means ± SEM. *P < 0.05, **P < 0.01, ***P < 0.001, ****P < 0.0001. Statistical analyses were performed using two-way ANOVA followed by Tukey's post hoc test.

profiles (Fig. 5F). Hierarchical clustering showed that genes associated with myeloid cell differentiation, cell migration, cytokine signaling pathways, the inflammatory response, and the hematopoietic response, such as *Adrb2*, *Gata1*, *Trem1*, *Igf2*, *Nlrp3*, and *Kitl*, were significantly up-regulated in the bone marrow of aged TBI mice (Fig. 5G). Visualization of the fragments per kilobase of exon per million mapped fragments (FPKM) of *Adrb2*, *Nlrp3*, and *Kitl* further confirmed their up-regulation after TBI, which was more pronounced in aged TBI mice than young TBI mice (Fig. 5H). Gene Ontology (GO) analysis of enriched biological processes revealed that genes up-regulated in the bone marrow of aged TBI mice were associated with leukocyte proliferation and development, immune system response, and positive regulation of hematopoiesis (Fig. 5I). Similarly, Kyoto Encyclopedia of Genes and Genomes (KEGG) enrichment analysis showed that the genes up-regulated in the bone marrow of aged TBI mice were involved in hematopoietic cell lineage differentiation, the adenosine monophosphate–activated protein kinase signaling pathway, the TNF signaling pathway, the nuclear factor kappa B signaling pathway, and other hematopoietic and inflammation-related signaling pathways (Fig. 5J). Gene set enrichment analysis (GSEA) showed that aged mice exhibited enhanced activity of pathways associated with myelopoiesis after TBI, including genes related to myeloid cell differentiation and up-regulated adrenergic receptor signaling pathway activity. Conversely, immunoregulatory interactions were significantly up-regulated in the bone marrow of young TBI mice (Fig. 5K).

To confirm the up-regulation of *Adrb2* in bone marrow of aged mice and determine whether other adrenergic receptors are involved, we examined the transcript levels of a battery of adrenergic receptors in bone marrow samples from mice and human specimens after TBI by quantitative reverse transcription polymerase chain reaction (qRT-PCR). The results demonstrated that β2 receptor–related genes (*Adrb2* and *ADRB2*) were the only genes up-regulated in both aged mice and patients after TBI compared to their young controls (Fig. 5, L and M). Detection of *Adrb2*-expressing cell types in the bone marrow of mice after TBI showed that *Adrb2* was widely expressed in bone marrow HSCs and precursors (fig. S13A).

We then tested whether β2 adrenergic receptor is responsible for abnormal bone marrow hematopoiesis in aged mice after TBI by generating *Adrb2* knockout mice ($Adrb2^{-/-}$). Flow cytometry results suggested that the number or frequency of bone marrow LSK cells before and after TBI were comparable between $Adrb2^{-/-}$ and wild-type (WT) mice, suggesting that *Adrb2* deficiency has no impact on the proliferation of HSCs or progenitor cells in mice (Fig. 6A). Nevertheless, the TBI-induced up-regulation of myeloid progenitors in bone marrow and increased neutrophil and $Ly6C^{high}$ monocyte output were inhibited in both aged and young $Adrb2^{-/-}$ mice. $Ly6C^{low}$ monocyte response was greater in both young and aged $Adrb2^{-/-}$ mice after TBI than in WT mice (Fig. 6, B to H). There were fewer brain-infiltrated neutrophils and $Ly6C^{high}$ monocytes in $Adrb2^{-/-}$ mice, but the numbers of $Ly6C^{low}$ monocytes were increased (Fig. 6I). *Adrb2* knockout resulted in positive gains in TBI mice of different ages, as evidenced by the up-regulation of macrophage immunomodulatory function, decreased concentrations of proinflammatory cytokines (TNF-α and IL-1β), and increased concentrations of anti-inflammatory cytokines (IL-4 and IL-10) in peripheral blood (Fig. 6, J and K). Both young and aged $Adrb2^{-/-}$ mice showed better recovery of neurological deficits after TBI, with smaller lesions on MRI (Fig. 6, L to N).

To further clarify the role of *Adrb2* of hematopoietic cells on myelopoiesis, we constructed four bone marrow chimeric mouse models to determine whether *Adrb2* acts in the hematopoiesis compartment to influence myelopoiesis in TBI as shown in fig. S14. Compared to WT-WT and WT-$Adrb2^{-/-}$ chimeric mice, deficiency of *Adrb2* in bone marrow inhibited abnormal myelopoiesis after TBI, with reduced neutrophil and $Ly6C^{high}$ monocytes but increased $Ly6C^{low}$ monocytes (fig. S14, B to E). In addition, brain infiltration of neutrophils and $Ly6C^{high}$ monocytes were reduced in $Adrb2^{-/-}$WT and $Adrb2^{-/-}Adrb2^{-/-}$ chimeric mice after TBI (fig. S14F).

To further confirm the role of the β2 adrenergic receptor on abnormal myelopoiesis after TBI, we enhanced neural electrical activity in the CeA after TBI in $Adrb2^{-/-}$ mice by using AAV9-TH-hM3Dq (fig. S15A). Compared to that in WT mice, enhancement of CeA activity did not increase the number of myeloid progenitors in bone marrow of $Adrb2^{-/-}$ mice (fig. S15, B and C) or affect the number of neutrophils or $Ly6C^{high}$ monocytes in the bone marrow and brains but instead increased the number of $Ly6C^{low}$ monocytes (fig. S15, D and E).

Overall, these data demonstrated that increased adrenergic input in aged mice triggers abnormal bone marrow myelopoiesis via β2 adrenergic receptor, generic deficiency of *Adrb2* rebalanced bone marrow myelopoiesis and improved the outcome of TBI mice.

Pharmacologic inhibition of β2-adrenergic receptor rebalances bone marrow myelopoiesis and improves outcomes in aged TBI mice

We then aimed to test whether β2-adrenergic innervation can be developed as a drug target to improve the clinical outcome of aged TBI mice. We investigated the effects of the selective β2-adrenergic receptor inhibitor, ICI118551 on bone marrow myelopoiesis and TBI prognosis. Consistent with findings from $Adrb2^{-/-}$ mice, treatment with ICI118551 had no effect on the number of bone marrow LSK cells after TBI in mice but significantly suppressed myeloid progenitors and the generation of neutrophils and $Ly6C^{high}$ monocytes after TBI and enhanced $Ly6C^{low}$ monocytes population, with reduced brain infiltration of neutrophils and $Ly6C^{high}$ monocytes but enhanced $Ly6C^{low}$ monocytes, more regulatory macrophages in the CNS, higher concentrations of immune-modulatory cytokines, and lower concentrations of proinflammatory cytokines in the peripheral blood (Fig. 7, A to C, and fig. S16, A to D). ICI118551 treatment promoted the recovery of sensorimotor function and reduced lesion size in both aged and young mice after TBI. In addition, ICI118551 treatment reduced the mortality of TBI mice (Fig. 7, D to F) and improved the learning and memory function during the chronic phase, with improved long-duration potentiation potential (LTP) (Fig. 7, G to M, and fig. S17). These data suggest that pharmaceutical inhibition of β2-adrenergic rebalances myelopoiesis and improves outcomes in both aged and young TBI mice.

DISCUSSION

Bone marrow is involved in the process of damage repair following acute brain injury by enhancing the output of nonclassical monocytes (*10*, *12*). This study demonstrates an abnormal myelopoiesis in aged patients with TBI, characterized by impaired output of nonclassical monocytes accompanied by increased output of neutrophils and classical monocytes, which potentially contribute to the poorer neurological outcome of older patients.

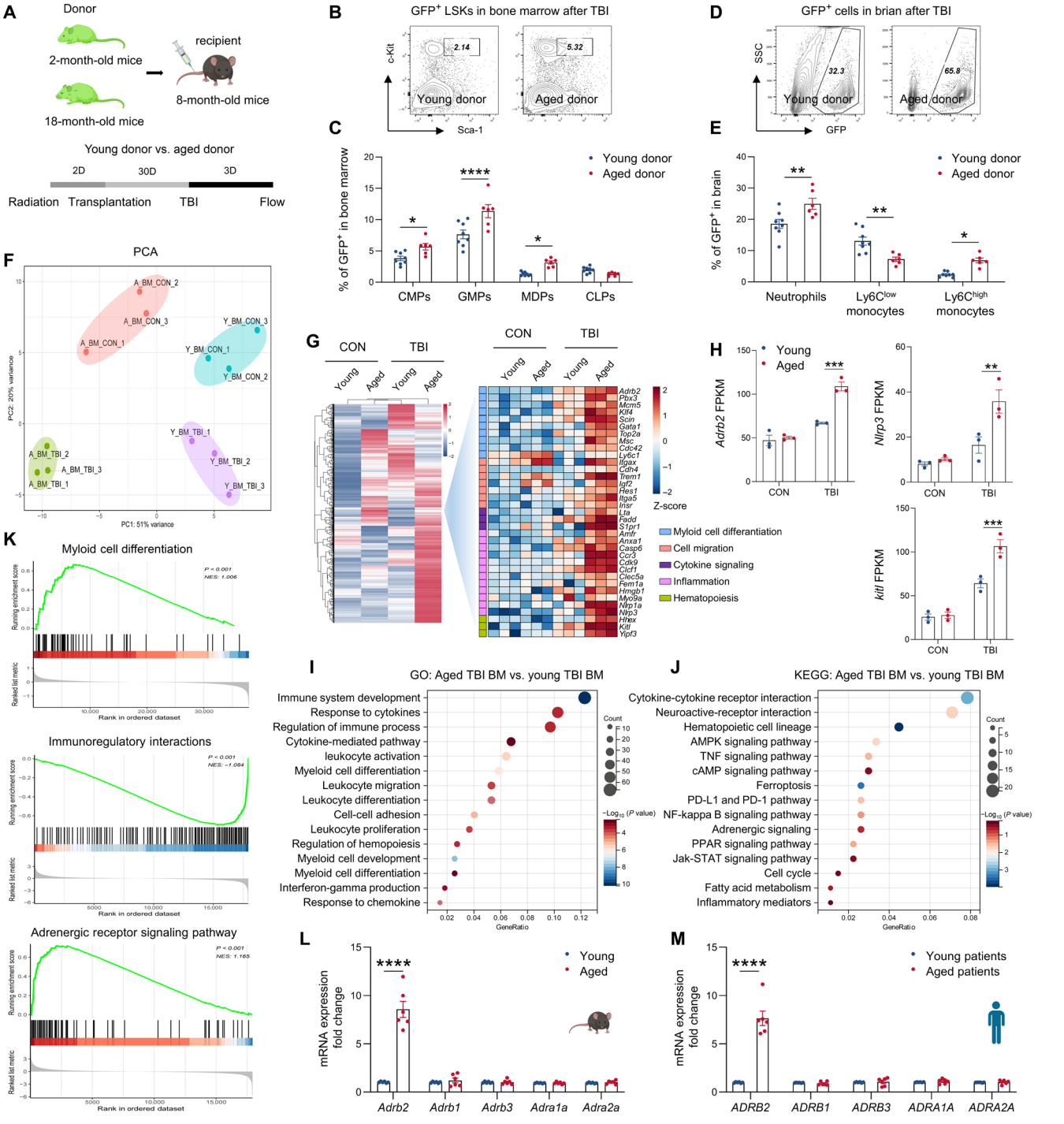

Fig. 5. Increased adrenergic β2 receptor signaling in aged bone marrow after TBI. (**A**) Schematic illustration shows the experimental design (created with BioRender.com). (**B**) Flow cytometry detection of LSKs in bone marrow of recipient mice receiving young or aged bone marrow transplantation. (**C**) Bar plot shows the proportions of GFP$^+$ CMPs, GMPs, MDPs, and CLPs in recipient bone marrow. (**D** and **E**) Flow cytometry plots and bar plot show the proportions of GFP$^+$ neutrophils, Ly6C^{low} monocytes, and Ly6C^{high} monocytes in recipient brains. (**F**) PCA analysis of bone marrow RNA sequencing of young and aged mice. (**G**) Heatmaps show that genes related to myeloid cell differentiation, cell migration, cytokine signaling, inflammation, and hematopoiesis were enriched in the bone marrow transcriptome of aged TBI mice. (**H**) Bar plots show FPKM values for *Adrb2*, *Nlrp3* and *Kitl*. (**I**) GO analysis based on genes up-regulated in bone marrow of aged TBI mice compared to the bone marrow transcriptome of young TBI mice. (**J**) KEGG analysis of genes up-regulated in aged TBI mice. (**K**) GSEA of genes up-regulated in aged TBI mice. (**L**) Bar plot shows the transcript levels of genes encoding adrenergic receptors in the bone marrow. (**M**) Bar plot shows the transcript levels of genes encoding adrenergic receptors in the bone marrow. $n = 6$ per group for (C), (E), and (L) to (M); $n = 3$ per group for (F) to (J). Data are represented as means ± SEM. *$P < 0.05$, **$P < 0.01$, ***$P < 0.001$, ****$P < 0.0001$. Statistical analyses were performed using two-way ANOVA followed by Tukey's post hoc test.

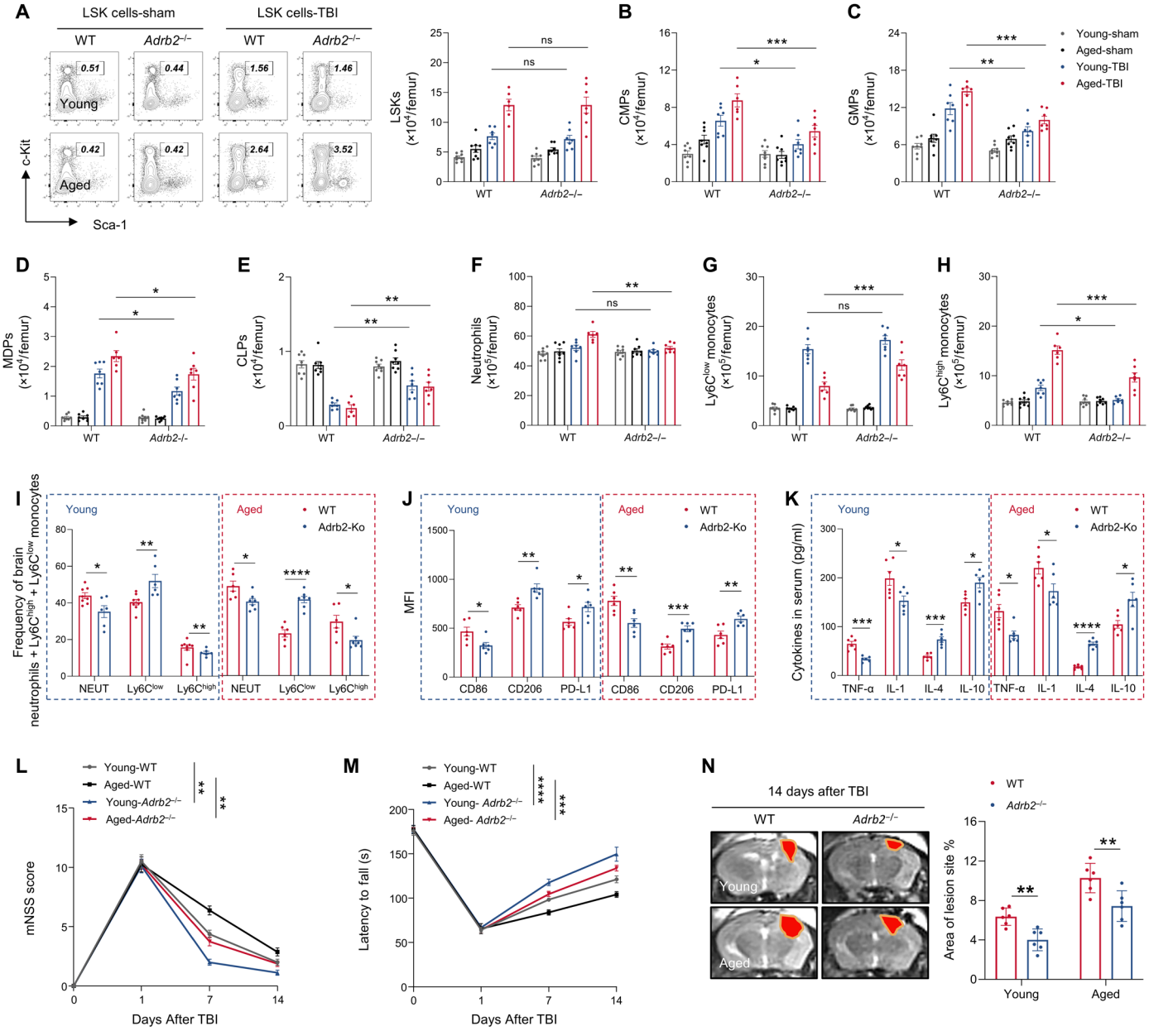

Fig. 6. β2-adrenergic receptor mediates abnormal myelopoiesis in aged bone marrow after TBI. (**A**) Flow cytometry plots and bar plots show changes in the number of LSKs in the femoral bone marrow before and after TBI in aged and young WT mice and *Adrb2*$^{-/-}$ mice. (**B** to **H**) Bar plots show changes in the numbers of LSKs, CMPs, GMPs, MDPs, CLPs, neutrophils, Ly6C^{low} monocytes, and Ly6C^{high} monocytes in the femoral bone marrow before and after TBI in aged and young WT and Adrb2$^{-/-}$ mice. (**I**) Bar plots show changes in the proportions of neutrophils, Ly6C^{low} monocytes, and Ly6C^{high} monocytes after TBI in aged and young WT mice and *Adrb2*$^{-/-}$ mice after TBI. (**J**) mean fluorescence intensity (MFI) of indicated molecules in macrophages of aged and young WT and *Adrb2*$^{-/-}$ mice after TBI. (**K**) Bar plots show changes in cytokine levels in the peripheral blood of aged and young WT mice and *Adrb2*$^{-/-}$ mice after TBI. (**L**) mNSS of aged and young WT mice and *Adrb2*$^{-/-}$ mice after TBI. (**M**) Fall latency of the rotarod test after TBI in aged and young WT mice and *Adrb2*$^{-/-}$ mice. (**N**) Magnetic resonance (MR) images of aged and young WT mice and *Adrb2*$^{-/-}$ mice on day 14 after TBI and quantitative analysis. $n = 6$ per group. Data are represented as means ± SEM. *$P < 0.05$, **$P < 0.01$, ***$P < 0.001$, ****$P < 0.0001$, Statistical analyses were performed using two-way ANOVA followed by Tukey's post hoc test.

Nonclassical monocytes are usually converted from classical monocytes (*19*, *20*). However, HSC lineage–tracing data suggest that newborn Ly6C^{low} monocytes were increased in the bone marrow after TBI, but not Ly6C^{high} monocytes, demonstrating that the population of Ly6C^{low} monocytes is enhanced after TBI, although we could not clarify whether Ly6C^{low} monocytes are generated separately.

The frequency of myeloid progenitor cells in the bone marrow rises significantly to fulfill the requirement of a large myeloid cell output, which is again more pronounced in aged patients with TBI. To gain mechanistic insight into these clinical findings, we conducted a comprehensive investigation in TBI mice. These experiments revealed that abnormal myelopoiesis after TBI is driven by enhanced adrenergic inputs to the CeA–bone marrow axis in a β2-adrenergic

receptor–dependent manner in the aged. Selective pharmacological blockade of β2-adrenergic receptors rebalances abnormal myelopoiesis and improves prognosis in aged mice after TBI.

HSCs continually replenish immune cells, and this replenishment is especially critical for shorter-lived immune cells such as granulocytes and monocytes (*21*). During aging, blood cell production shifts to myeloid cells at the expense of lymphocytes, a change that has been associated with a higher risk of a variety of myeloid-related conditions, such as myelodysplastic syndromes and leukemia (*22*, *23*). Our data suggest that myeloid hematopoiesis is significantly up-regulated during emergency hematopoiesis mobilized by the bone marrow after TBI, a phenomenon that is particularly evident in aged patients with TBI. Along with bone marrow, the spleen can induce mononucleosis under conditions of psychological stress. Chronic social stress in mice leads to splenomegaly, attributed to granulocyte accumulation and extramedullary hematopoiesis, which increases circulating monocyte populations (*24*). However, our study identified significant suppression of extramedullary hematopoiesis (in the peripheral blood and spleen) after TBI, which was particularly pronounced in aged mice. This finding is consistent with previous reports (*15*). At the molecular level, aged bone marrow after TBI up-regulates the expression of genes associated with the stress response and inflammation, as well as genes involved in myeloid differentiation. Previous studies demonstrated that in the physiological state, compared to aged HSCs, young HSCs exhibit increased self-renewal–related gene expression, that is, HSC exhaustion is a hallmark of aging immunity (*25*–*27*). However, the activation of bone marrow HSCs in aged patients after TBI suggests that more features of pathologically aged bone marrow still need to be explored.

Aging of the immune system is associated with dramatic changes in the distribution and functional properties of immune cells (*28*). Nonclassical patrolling monocytes can repair cerebrovascular units, suppress neuroinflammation, and improve neurological outcomes (*20*, *29*). We found that bone marrow impairs the output of nonclassical monocytes in aged patients, potentially contributing to the poorer prognosis of aged patients. Complex cellular and molecular cues coordinated between hematopoietic stem and progenitor cells (HSPCs), perivascular stromal cells, and the autonomic nervous system, particularly sympathetic noradrenergic nerve fibers, control HSPC proliferation, regeneration, and differentiation (*30*). Increased β2-adrenergic signaling during aging promotes myeloid expansion (*17*). Our results suggest that aging-induced impairment of nonclassical monocyte output is dependent on β2-adrenergic receptor signaling. Both aged mice and patients exhibited a dramatic increase in NE in bone marrow after TBI compared with young mice and patients. Imaging of thick bone sections in this study demonstrated that the density of adrenergic fibers was significantly increased in the bone marrow after TBI, which was particularly evident in aged mice. However, the enhanced sympathetic response in *Adrb2*$^{-/-}$ mice after TBI does not result in abnormal myelopoiesis or impaired output of nonclassical monocytes, suggesting that it is a neurotransmission-induced pathologic change (β2-adrenergic receptor) rather than a result of the generalized enhancement of sympathetic innervation of the bone marrow during aging after TBI. Previous reports also support our view: Shi *et al.* (*10*) reported that enhanced bone marrow sympathetic innervation in young patients with intracerebral hemorrhage (ICH) promotes the output of nonclassical monocytes and thus aids in the repair of brain injury. The study by Liu *et al.* (*12*) on the prognosis of patients with TBI combined with fractures similarly found that enhanced sympathetic bone marrow innervation after TBI in young mice promoted the population of nonclassical monocytes and M2-like macrophages, which in turn facilitated fracture repair. Notably, activation of the hypothalamic pituitary adrenal (HPA) axis promotes the proliferation of myeloid progenitor cells and induces inflammatory myelopoiesis (*31*), and the difference in HPA axis viability after TBI may synergize with enhanced sympathetic innervation of the bone marrow, which together contribute to the poor prognosis of aged patients with TBI. This possibility warrants further investigation.

The central control of autonomic nervous system functions, such as respiration and digestion, has been extensively studied, but the specific neuronal populations involved in the top-down brain-body circuits that regulate systemic immune responses are less well understood (*32*). Available data suggest that after PRV infection of bone marrow, the virus spreads to areas such as the bed nucleus of the stria terminalis, the arcuate nucleus of the hypothalamus, and the amygdala, demonstrating extensive innervation of the bone marrow by the CNS and that the CeA can modulate the immune response in the spleen through the HPA axis (*33*, *34*). Although we do not have direct evidence of activation of CeA regions in other types of brain injury, there are studies that report that TBI (*12*); stroke, both ischemic stroke (*35*) and ICH (*10*); atherosclerosis (*36*); and even fractures (*12*, *37*), orchestrate bone marrow myelopoiesis, which is similar to what we observed in TBI, implying similar mechanisms underlying myelopoiesis after acute brain injury. In this study, evidence from retrograde and anterograde tracking of viruses combined with calcium imaging suggests the presence of a CeA–bone marrow axis. CeA–bone marrow axis–dominated adrenergic hypersensitivity mobilizes emergency hematopoiesis and results in abnormal myelopoiesis as well as impaired population of nonclassical monocytes. Although chemical-genetic approaches to intervene in the electrical activity of the CeA region before TBI used in this study is not sufficient enough to recapitulates the responses after TBI, it provides evidence that the activity of neurons in CeA region is directly responsible to bone marrow responses to acute brain injury as we observed in this study, which provide direct evidence for the connections between brain and bone marrow. The suppression of the electrophysiological activity of CeA after TBI showed good therapeutic potential, and the correction of abnormal myelopoiesis with the restoration of nonclassical monocyte output greatly contributed to the recovery of neurological function in TBI mice, especially in aged TBI mice.

MATERIALS AND METHODS

Human bone marrow and brain samples

Human studies were conducted in accordance with the Declaration of Helsinki. The inclusion of human subjects and supporting documentation were approved by the Ethics Committees of the Affiliated Hospital of Nantong University (approval no. 2023-K187-01). Informed consent was obtained from all subjects or a legally acceptable surrogate at the time of enrollment. Contusion brain tissue and skull bones were collected from patients with TBI who underwent hematoma removal and decompressed craniectomy.

Skull samples were taken from the operating room to the laboratory on ice. The sample was cut into thinner, smaller pieces using a chainsaw. Using a syringe, bone marrow cells were rinsed with phosphate-buffered saline (PBS) into a 50-ml tube. The bones were

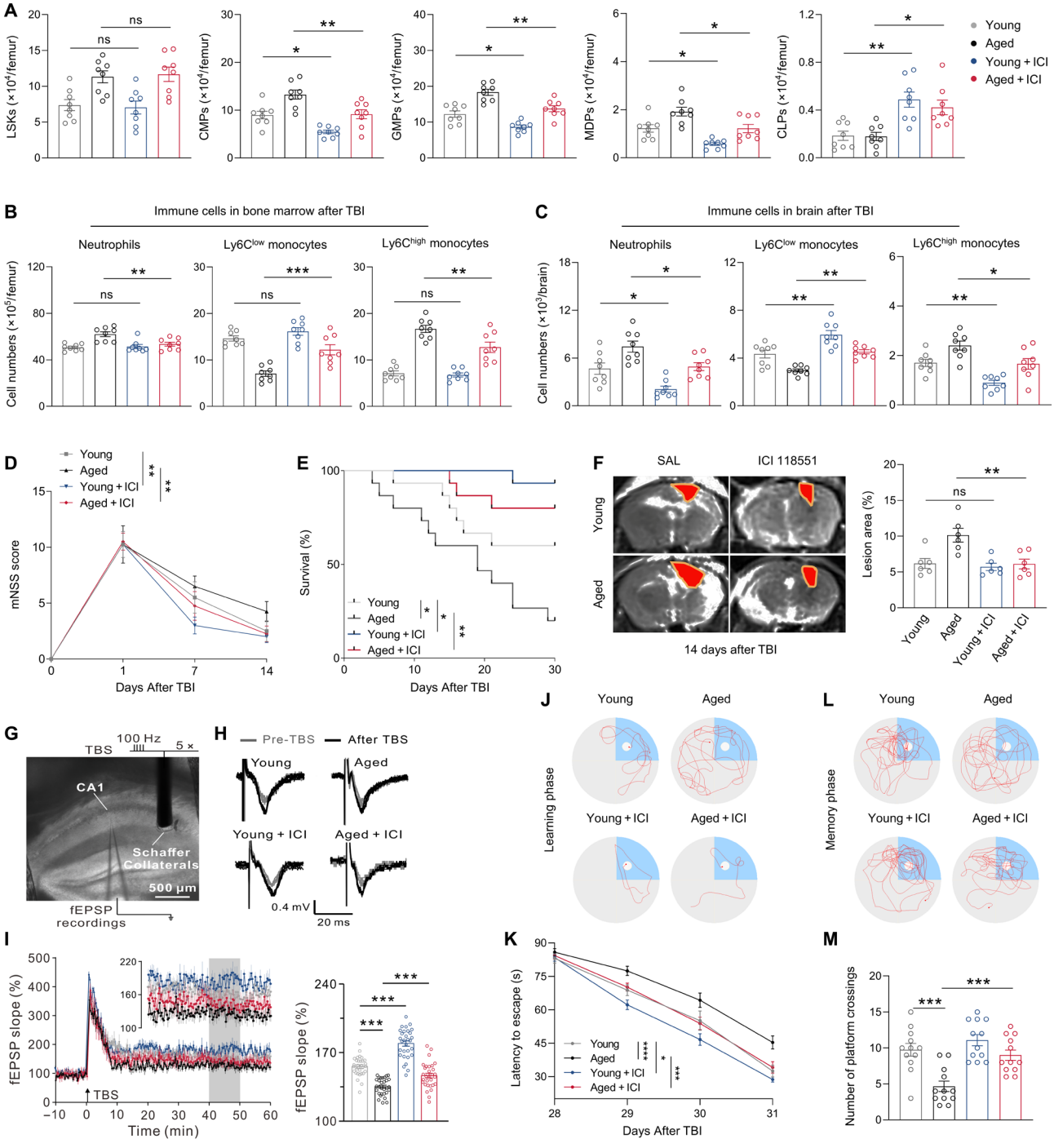

Fig. 7. Pharmacologic inhibition of β2-adrenergic receptor–rebalanced bone marrow myelopoiesis after TBI. (**A**) Bar plots show changes in the number of LSKs, CMPs, GMPs, MDPs, and CLPs in the bone marrow after TBI. (**B**) Bar plots show changes in the number of neutrophils, Ly6C^{low} monocytes, and Ly6C^{high} monocytes in the bone marrow after TBI. (**C**) Bar plots show changes in the numbers of neutrophils, Ly6C^{low} monocytes, and Ly6C^{high} monocytes in the brains after TBI. (**D**) Changes in the mNSS scores. (**E**) Survival curves of mice in indicated groups from model induction to 30 days after injury. (**F**) MR images of the brain lesion and quantitative analysis. (**G**) Schematic of the stimulation and recording configuration demonstrating LTP induction at Schaffer collateral-CA1 synapses. (**H** and **I**) Representative traces, normalized field excitatory postsynaptic potential (fEPSP) slopes, and average fEPSP slopes (at 40 to 50 s) were recorded from hippocampal slices of young and aged mice injected with the β2 adrenergic antagonist ICI 118551 (intraperitoneally.). (**J**) Representative trajectories for each group in the learning phase of Morris water maze (MWM). (**K**) Line plot shows changes of the latency to escape during MWM training phase. (**L**) Representative trajectories for each group in the detection test. (**M**) Bar plot shows the number of platform crossings in the MWM test. $n = 6$ per group for (F). $n = 8$ per group for (A) to (D). $n = 12$ to group for (K) and (M). $n = 15$ per group for (E). $n = 30$ per group for (I). Data are represented as means ± SEM. *$P < 0.05$, **$P < 0.01$, ***$P < 0.001$, ****$P < 0.0001$. Statistical analyses were performed using one-way ANOVA followed by Tukey's post hoc test (A to C, F, I, and M), Kaplan-Meier survival analysis (E) and two-way ANOVA followed by Tukey's post hoc test (D and K).

further pulverized using a mortar and pestle on ice to release more bone marrow cells into the cell suspension. All the samples were filtered through a 70-μm strainer. Human bone marrow cells were isolated by centrifugation in Ficoll (Sigma-Aldrich) to remove red blood cells and bone debris.

The brain tissue was minced and incubated with collagenase IV and deoxyribonuclease at 37°C for 30 min. After removal of myelin debris by centrifugation in 30% Percoll, single cells were suspended in 1% bovine serum albumin.

A total of 26 young (18 to 45 years old) and 29 aged (>65 years old) subjects were included in the study. Patient characteristics are listed in table S1.

Human blood samples

Handling of human blood followed the Declaration of Helsinki. The inclusion of human subjects and supporting documentation were approved by the Ethics Committees of the Affiliated Hospital of Nantong University. Blood samples were collected from 38 young (18 to 45 years old) and 37 aged (>65 years old) patients at 1, 3, and 7 days after TBI (surgically or conservatively treated). Patient characteristics are listed in table S2. Exclusion criteria for both patients with TBI and healthy control subjects included infections, immunological disorders, immunosuppressive medication, pregnancy or nursing, and previous neurological disorders that could confound the evaluation of TBI-related neurological sequelae. Human peripheral blood mononuclear cells were isolated from whole blood by centrifugation using human peripheral blood lymphocyte isolation medium (Beyotime, C0025).

Mice

Adrb2$^{-/-}$ mice (catalog no. NM-KO-190738) and CAG-GFP-Tg mice (catalog no. NM-TG-00005) were purchased from the Shanghai Model Organisms Center. Young (6 to 12 weeks) and aged (18 to 24 months) male WT C57BL/6 mice were bred and aged in house purchased from Chengdu Dossy Experimental Animals Co. Ltd. Experimental mice were kept in an air-conditioned room (Temp: 22° to 25°C) with a standard 12-hour light/dark cycle and free access to food and water. The United States' National Institutes of Health Guide for the Care and Use of Laboratory Animals was followed for all animal experiments, and the experimental procedures were approved by the Experimental Animal Ethics Committee of Nantong University (approval no. IACUC20231125-1001).

TBI model

A CCI model was used to induce TBI in mice as described (*38*). Briefly, after successful induction of anesthesia in mice using a 2.5% mixture of isoflurane and oxygen, the mixture was changed to 1.5% to maintain anesthesia. The mouse's head was then fixed in the stereotactic frame with a hot pack placed under the body to keep the body temperature at 37°C. A median incision was made on the scalp, and a 2-mm-diameter bone window was created 2.0 mm lateral to the median sagittal line and 1.0 mm posterior to the bregma. The brain was tilted at an angle of 15° and placed perpendicular to the impactor (4-mm-diameter tip; RWD Life Science, China). The impactor parameters for CCI were impact speed, 3.5 m/s; deformation depth, 1.30 mm; and duration, 400 ms. After CCI, the skin incision was sutured and treated with antibiotic ointment to prevent infection. The mice were placed on a heating pad to keep the core body temperature up until they had recovered from anesthesia. For the sham group, a craniotomy was also performed, and the dura was exposed, but no impact was made.

HSC lineage tracing

Fgd5-CreER-tdTomato reporter mice were used to track HSC differentiation. Fgd5-creER-tdTomato mice were given intraperitoneal injection of tamoxifen for three consecutive days, and the TBI model was induced 2 days later. After 3 days, the mice were euthanized and their bone marrow was harvested for flow cytometry.

qRT-PCR

After tissue disruption and homogenization in 1 ml of QIAzol, along with 200 μl of chloroform and vortexing for 15 s, RNA extraction from the bone marrow was conducted using QIAzol (Qiagen, Germany). To achieve phase separation, the samples were allowed to sit at room temperature for 10 min before being centrifuged for 10 min at 12,000*g* at 4°C. The upper layer, which contained the RNA, was meticulously transferred to a separate tube and precipitated with an equal volume of isopropanol. After centrifugation for 10 min at 8000*g* at 4°C, the ethanol was removed from the samples, which were air-dried. The RNA pellet was reconstituted in 20 μl of ribonuclease (RNase)–free dH_2O. The concentration of RNA was determined using a NanoDrop spectrophotometer. For reverse transcription, 0.75 mg of RNA (diluted in a total volume of 40 μl of dH_2O) was incubated at 70°C for 10 min with 5 μl of random hexamers (Biomers, Germany). The samples were then cooled on ice, and a master mixture containing 0.5 μl of reverse transcriptase (Promega, Germany), 0.5 μl of RNase inhibitor (RiboLock, Thermo Fisher Scientific, Germany), 2 μl of deoxynucleotide triphosphates (Genaxxon, Germany), and 12 μl of reverse transcriptase buffer (Promega, Germany) was added. The samples were incubated at ambient temperature for 10 min and then transferred to a water bath set at 42°C for 45min. The samples were incubated for 3 min, after which they were placed on ice for preservation and future use.

The primers used in this study were developed through the use of the NCBI Primer-BLAST program, which is affiliated with the United States National Center for Biotechnology Information. The corresponding sequences were acquired by using the NCBI nucleotide search tool GenBank. The Primer-BLAST tool was used to fine-tune the parameters to optimize the PCR yield for the in-house light cycler, specifically the Roche Light Cycler 480 II. To summarize, the range of the PCR product size was established as 70 to 140, the primer melting temperature (Tm) was determined to be 60° ± 3°C, no specific preference was given to the exon junction span, and the appropriate organism (*Mus musculus*) was chosen. The primer pair exhibiting the highest Tm, self-complementarity, and self-3′ complementarity was selected, and the primer pairs were verified for specificity toward the target gene using Primer-BLAST tool. Before we used them in experiments, we validated the primers by conducting a test sample alongside the appropriate controls (samples lacking RNA and samples lacking reverse transcriptase) to confirm the Ct value, thereby ensuring primer selectivity and functionality. Full primer sequences for each gene examined can be found in table S3.

For each sample, RNA (2 μg) was subjected to reverse transcription using the TMRT kit (Takara Bio Inc., Japan). qRT-PCR was conducted on an ABI QuantStudio5 Q5 real-time PCR system (Thermo Fisher Scientific, USA) using SYBR Green (Roche, Germany). The

$2^{-\Delta\Delta Ct}$ method was used to determine and standardize relative mRNA expression with respect to glyceraldehyde-3-phosphate dehydrogenase expression.

Flow cytometry

Mice were euthanized by isoflurane lethal anesthesia, after which the brain and femur were removed. The cerebral hemisphere on the injured side was isolated, minced, and incubated with collagenase IV and deoxyribonuclease for 30 min at 37°C. After removal of myelin fragments by centrifugation in 30% Percoll, single cells were suspended in 1% bovine serum albumin for antibody staining. For mouse bone marrow, the marrow was flushed from the femur through PBS using a syringe. After the bone marrow fluid was filtered through a 70-μm strainer, erythrocytes were removed using red blood cell lysis buffer (Beyotime, C3702). Antibody staining was performed after resuspending single cells in 1% bovine serum albumin. Human samples were stained after obtaining single-cell suspensions as described. For intracellular staining, the cells were fixed in fixation buffer for 20 min after surface marker staining. After washing twice in permeabilization buffer, the cells were incubated with antibodies in staining buffer for 45 min (see table S4 for antibodies). The data were collected by an FACSAria III flow cytometer and were analyzed using FlowJo software.

Enzyme-linked immunosorbent assay

The serum levels of NE, TNF-α, IL-1β, IL-4, and IL-10 in patients and mice were measured using commercial enzyme-linked immunosorbent assay (ELISA) kits according to the manufacturer's instructions. The ELISA kits used are listed below:

NE (Elabscience, E-EL-0047c), mouse TNF-α ELISA kit (Multi Sciences, 70-EK182-96), mouse IL-1β ELISA kit (Multi Sciences, 70-EK101B-96), mouse IL-4 ELISA kit (Multi Sciences, 70-EK104/2-96), mouse IL-10 ELISA kit (Multi Sciences, 70-EK110/2-96), human TNF-α ELISA kit (Multi Sciences, 70-EK282-96), human IL-1β ELISA kit (Multi Sciences, 70-EK201B/3-96), human IL-4 ELISA kit (Multi Sciences, 70-EK204/2-96), and human IL-10 ELISA kit (Multi Sciences, 70-EK210/4-96) were used.

Immunofluorescence staining

Freshly dissected mouse femurs or human skulls obtained during debridement surgery were fixed in 4% paraformaldehyde (PFA) for 12 hours at 4°C and washed several times in PBS. The bones were decalcified in PBS containing 10% EDTA and 30% sucrose with continuous agitation for 2 to 4 weeks. For brain immunohistochemistry, samples were fixed directly in 4% PFA. The samples were dehydrated in 30% sucrose, embedded in OCT compound (Tissue-Tek), and stored at −20°C until further processing. Sections of bone were cut into 20-μm sections and brain tissue into 10-μm sections using a slicer (Leica). Bone sections were permeabilized with Hanks' balanced salt solution (HBSS) containing 0.05% NP-40 and 2.5% dimethyl sulfoxide (DMSO) for 10 min. Brain sections were treated with quick antigen retrieval solution for frozen sections (Beyotime, P0090) for 30 min. After washing with PBS, the sections were blocked in PBS containing 5% normal donkey serum (Jackson Nutrition) for 2 hours. The sections were then stained and incubated overnight at 4°C. After incubation with secondary antibodies, the nuclei were stained with 4,6-diamidino-2-phenylindole (C0060, Solarbio). The sections were sealed with antifading mounting medium (S2100, Solarbio). Images were acquired using the Navigator function of the Leica Thunder 3D Assay inverted fluorescence microscope and then stitched together using LAS X software to create a composite image of the tissue. Images were processed and analyzed using Fiji (ImageJ) and Photoshop (Adobe Systems). The list of antibodies used can be found in table S4.

Retrograde tracing of PRV from bone marrow

PRV-CAG-RFP was prepared as a stock of 10^9 genomic copies/ml. Mice were anesthetized by intraperitoneal injection of 1% pentobarbital sodium. After shaving and disinfecting the skin on the surface of the femur, the skin on the outer surface of the femur was carefully cut with clean surgical scissors, and the muscle layer on the surface of the femur was bluntly separated with clean ophthalmic forceps to expose the femur. A 1-ml syringe was used to carefully drill holes in the target area of the femur until a hole about 100 μm in diameter was removed. Each mouse was injected with 3 μl of virus solution using a microsyringe. The polished hole was filled with erythromycin ointment, and the muscle layer and skin were carefully stitched. The state of the animals was observed every day, and the heart was perfused with PBS and 4% PFA after the experimental animals showed obvious neurological symptoms. The brain and spinal cord were removed and fixed after soaking in 4% PFA for more than 24 hours, and then the solution was replaced with 30% sucrose solution for more than 48 hours. The samples were then frozen and sliced. The frozen sections were washed with PBS (three times, 5 min each) and stained with 4′,6-diamidino-2-phenylindole. An OlympusVS200 microscope was used to collect and export the images. Different brain regions were identified using the Allen Mouse Brain Atlas (https://mouse.brain-map.org/), and the mouse brain regions were identified in stereotactic coordinates.

HSV tracking downstream from the CeA

HSV-TH-GFP was prepared as a stock solution of 10^9 genomic copies/ml. Adult B6 mice were anesthetized with sodium pentobarbital (75 mg/kg). A total of 0.2 μl of viral stock solution was injected through brain stereotaxic localization in the CeA of mice [fontanel coordinates: −1.23 mm anterior-posterior (AP), ±2.75 mm medial-lateral (ML), and −3.9 mm dorsal-ventral (DV)] using a Hamilton 0.5-μl syringe. The surgical wounds were closed with standard sutures, and the indicated number of mice was euthanized after 72 hours to remove the femur, spinal cord, and brain. Sections were prepared and processed to identify HSV-GFP^+ neurons in different regions. The sections were processed and photographed as described in the Immunofluorescence section.

Stereotactic surgeries and virus injection

Brain surgery was performed under aseptic conditions by placing 20 to 25 g mice in stereotaxic frames (1404, David Kopf Instruments, Tujunga, CA). Mice were induced with 4% isoflurane (RWD Life Science Co. Ltd., R510-22-10) and maintained on 1.5% isoflurane during surgery. Then, 1 to 2 cm of the scalp was cut to expose the skull. A small hole was drilled in the skull, and the dura was gently opened to allow the micropipette to pass through without interruption. For fiber photometry, the adeno-associated virus rAAV-hSyn-NES-jRGECO1a-WPRE-hGHpA (0.1 μl, titer: 2.76×10^{13} v.g. ml^{-1}, BrainVTA Company, Wuhan) was injected into the right-hemisphere CeA (AP, −1.23 mm; ML, 2.75 mm; DV, −3.9 mm), PVN (AP, −1.06 mm; ML, 0.00 mm; DV: −2.40 mm), and ZI (AP, −2.54 mm; ML, 1.65 mm; DV: −3.65 mm).

Fiber photometry

Three weeks after virus injection, an optical fiber (200 μm, 0.37 NA; Inper) was implanted 100 μm above the CeA, PVN, and ZI. Neurons expressing jRGECO1a were stimulated in free-moving mice using a fiber photometry system (ThinkerTech Nanjing Bioscience Inc., QAXK-FPS-MC-LED) to obtain calcium-dependent fluorescence signals. The laser intensities for the 580-nm-wavelength bands (~60 μW) and the 405-nm signal (20 μW) were used to correct movement artifacts. The raw signals were demodulated and analyzed using custom-written software in MATLAB. The recordings lasted for 1 min and were taken at 6-hour intervals before TBI and for 7 days after TBI. To calculate the jRGECO1a signal, we calculated the relative changes in the fluorescence of $\Delta F/F$ as the Ca^{2+} signal using the formula $\Delta F/F = (F-F0)/^{F}0$, where $F0$ represents the fluorescence of the same mouse before TBI.

Chemogenetics

For chemical stimulation of TH neurons in the CeA, AAV2/9-TH-hM3Dq or AAV2/9-TH-hM4Di viruses or control viral vectors were injected by brain stereotaxic localization in the CeA of young and aged mice (fontanel coordinates: −1.23 mm AP, ±2.75 mm ML, and −3.9 mm DV). AAV2/9-TH-hM3Dq or AAV2/9-TH-hM4Di was supplied by Shanghai Giga Gene Technology Co. After the animals were allowed to recover from surgery for 21 days, they were continuously fed DCZ for 7 days, after which TBI modeling was performed.

Patch clamp recordings in vitro

Whole-cell patch-clamp recordings were performed as described (*39*–*42*). Mice weighing 20 to 25 g were decapitated under 4% isoflurane anesthesia for induction, and slices containing the CeA and hippocampus from adult male and female mice were identified using the mouse brain atlas and then incubated in oxygenated artificial cerebrospinal fluid [(ACSF, composition in mM: 125 NaCl, 25 $NaHCO_3$, 2.5 KCl, 1.25 NaH_2PO_4, 2 $CaCl_2$, 1.5 $MgCl_2$, and 10 D-glucose (pH 7.4) 300 to 310 mosmol] at 35° ± 0.5°C for at least 1 hour. The slices were kept at room temperature for approximately 30 min before recording. Then, they were moved to a submerged chamber during recording sessions and continuously perfused with oxygenated ACSF at a rate of 2 ml/min maintained at 32 ± 0.5°C.

Recordings were conducted using patch electrodes made of borosilicate glass that were pulled using a Flaming-Brown puller (Sutter Instruments, CA) and polished with a polishing tool (Narishige, Tokyo, Japan) immediately before use. The pipette resistance typically ranged from 4 to 6 megohm. The internal solution comprised the following (in mM): 135 $KMeSO_4$, 10 Na2-phosphocreatine, 5 KCl, 0.5 $CaCl_2$, 5 Hepes, 5 EGTA, 2 Mg_2ATP, and 0.5 Na_3GTP, adjusted to pH 7.25 with KOH. CeA neurons were observed using an Olympus BX51WI microscope (Tokyo, Japan) equipped with an infrared differential interference contrast and fluorescence module. All images were captured using a Hamamatsu ORCA FLASH4.0 camera (Hamamatsu Photonics, Japan) and displayed on a laboratory computer. Patch clamp recordings were obtained using an Axopatch-700B amplifier (Axon Instruments, Sunnyvale, CA) and fed into a computer via a Digidata-1440 interface (Axon Instruments) for data acquisition and analysis (pClamp 10.0, Axon Instruments). Recordings of whole-cell currents were filtered at a low-pass of 2 kHz and were digitized at 10 kHz, while recordings of membrane potentials were filtered at a low-pass of 5 kHz and were digitized at 20 kHz. Neurons were kept at a membrane potential of −70 mV and were assessed by injecting a rectangular voltage pulse (5 mV, 50 ms) to measure the whole-cell membrane capacitance, series resistance, and membrane resistance. Any neurons with unstable series resistance or a resistance exceeding 30 megohm were excluded from the study. Neurons with seal resistance changes of more than 30% of the initial level were also abandoned and excluded from further analysis.

The neuronal resting membrane potential was recorded under a current clamp (I = 0 pA). Input resistance was measured through potential changes resulting from injected currents ranging from −30 to 150 pA. The action potential was assessed by injecting a series of current pulses with an intensity of −30 to 150 pA, incrementing by 30 pA, and lasting for 1 s. For chemogenetic experiments, DCZ (MedChem Express, NJ, 0.05 μM) was dissolved in DMSO and added to ACSF at a final concentration of 0.3% DMSO (*43*, *44*).

Evaluation of neurological deficit

Neurological function was independently assessed by two investigators who were blinded to the treatment assignment. The neurological deficits of the mice were evaluated by the modified neurological severity score (mNSS), which comprehensively evaluates motor, sensory, reflex, and balance functions via a battery of tests. The mNSS ranges from 0 to 18; 13 to 18 indicates severe injury, 7 to 12 indicates moderate injury, and 1 to 6 indicates mild injury.

Rotarod test

Mice were trained on an accelerated (5 to 30 rpm) rotarod for 3 days. During the test phase, the mice were placed on an accelerating rotary rod with the speed increasing from 5 rpm to 30 rpm over 5 min. The latency of the mice to fall from the rod was recorded, and each mouse was trained for five trials (each trial ran for 5 min, followed by rest for 5 min). The final score was the average latency of the five falls of the experimental mice. Rotarod testing was performed 1 day before TBI and 1, 7, and 14 days after TBI. All experiments and data analyses were performed in a blinded manner.

Magnetic resonance imaging

Brain lesion size and perihematomal edema in TBI mice were evaluated with a 3-T small-animal magnetic resonance imaging scanner (GE Healthcare, Little Chalfont, Buckinghamshire, UK). T2-weighted images of the brain were acquired with fat-suppressed rapid acquisition with a relaxation enhancement sequence (repetition time, 4000 ms; echo time, 60 ms; slice thickness, 0.5 mm) to visualize lesion volume. The hematoma volume was visualized on susceptibility-weighted images (SWIs; repetition time, 21.0 ms; echo time, 8.0 ms; 0.3-mm thickness). T2 and SWI images were manually traced and calculated by summing the volume by the distance between sections via ImageJ (National Institutes of Health). Perihematomal edema volume was calculated as the difference between lesion and hematoma volumes (*10*). The magnetic resonance imaging data were analyzed by two researchers who were blinded to the experimental conditions.

Bone marrow chimeric mice

After the heads of the mature C57BL/6 mice were protected with a shield, the recipient mice were irradiated with two 4.5-gray [(Gy) 9 Gy total] doses of whole-body radiation using an XRAD 320 x-ray irradiator (Precision X-ray) at 4-hour intervals. The mice were then placed in cages and returned to the housing room. Polymyxin B and neomycin were added to the drinking water to prevent infection. Two

days later, the GFP donor mice were euthanized, and the femurs were isolated. Bone marrow hematopoietic cells were isolated by flushing femurs with 2% heat-inactivated bovine serum in Ca^{2+}- and Mg^{2+}-free HBSS (HBSS-free). The cells were dissociated into single-cell suspensions by filtration through a 70-μm nylon strainer. After the recipient mice were immobilized, approximately 5 million bone marrow cells per mouse were injected through the tail vein. TBI modeling was performed on recipient mice 2 weeks after transplantation.

mRNA sequencing of mouse bone marrow

Quality control of the sequence data was examined using FastQC, and the raw data were filtered with fastp to obtain high-base quality and adaptor-removed reads. Then, these clean reads were mapped to the *M. musculus* reference genome (UCSC mm10) using STAR Aligner, and reads that matched exactly more than once with equal quality were discarded. After alignment, the raw read counts for each gene were quantified by featureCount. PCA was performed to assess variance between sample groups and sample replicates. For differential gene expression analysis, DESeq2 was used to detect up-/down-regulated genes based on a negative binomial generalized linear model, and genes with a P value < 0.05 and an absolute fold change ≥ 2 were considered significantly differentially expressed. Next, GO and KEGG enrichment analyses were run on the differentially expressed genes via Metascape, and GO terms and KEGG pathways with $P < 0.05$ and gene count > 3 were considered significantly enriched. GSEA was performed using ClusterProfiler in R. A heatmap was generated with pheatmap to show the differentially expressed genes between groups, and a volcano plot with the genes labeled was generated with ggplot2.

Drug administration

ICI 118,551 (HY-13951, MedChemExpress) was diluted in saline and administered intraperitoneally at 10 mg/kg for 4 days. Tamoxifen (HY-13757A, MedChemExpress) was dissolved in ethanol/corn oil (1:9) at a concentration of 30 mg/ml, and Fgd5-creER-tdTomato mice received 100 μl (3 mg per mouse) daily for five consecutive days by intraperitoneal injection.

Stimulation and recording protocols for field recordings

Recordings began 1.5 to 2 hours after preparing coronal hippocampal slices with a thickness of 400 μm. Field excitatory postsynaptic potentials (fEPSPs) were recorded using a glass capillary microelectrode filled with 2 M NaCl, resulting in resistances ranging from 1 to 3 megohm in the stratum radiatum layer of the CA1 region. A concentric bipolar stimulating electrode (CBARC75, FHC, Bowdoin, ME) was used to administer 100- to 300-μs test pulses to the Schaffer collateral afferents. Low-frequency test stimulation was applied at a rate of 0.05 Hz once every 20 s. The stimulus intensity was set to elicit an fEPSP amplitude that was 40 to 50% of the maximum. Test responses were recorded for a minimum of 10 min before the experiment commenced to ensure response stability. A theta-burst stimulation (TBS; five sets of bursts, each with four pulses at intervals of 100 Hz and 200 ms) protocol was implemented to induce LTP. LTP strength was gauged by the slope of the fEPSP 60 min after the TBS stimulation.

Morris water maze test

Mice were subjected to the Morris water maze test 28 to 32 days after TBI. The water maze consisted of an open circular pool (diameter, 120 cm; depth 50 cm) filled with water, and the water temperature was 22° to 25°C. A small amount of nontoxic white additive was added to make the water opaque. The two vertical axes of the maze divided the pool into four quadrants. Various prominent visual cues were placed around the pool. A circular target platform (10 cm by 10 cm) was placed in the southeast quadrant and submerged 1 cm underwater. On four consecutive days of training, the mice were trained four times a day with a 30-min training interval. The starting direction for each trial was a different quadrant of the pool but was consistent for each mouse tested. When the mouse found the platform within 90 s, it was allowed to stay on the platform for 15 s. If the mouse did not find the platform within 90 s, it was guided to the platform and allowed to stay there for 30 s. During the exploration trial on day 5, the platform was removed, and each animal had 90 s to swim freely in the pool. EthoVisionXT software was used to track, record, and analyze the swims. The seconds of latency to escape and the number of times it crossed the platform location were recorded.

Statistical analysis

Plots and statistics were generated using GraphPad Prism 9.4.1 (GraphPad software). The data are shown as means ± SEM or means ± SD. Statistical parameters, including the number of mice, number of replicates, and statistical tests used, as well as P values, are indicated in each figure legend.

Ethics statement

The study was approved by the Ethics Committee of the Affiliated Hospital of Nantong University (approval no. 2023-K187-01). All participants provided written informed consent. All experimental procedures were in accordance with the Guidelines on the Care and Use of Laboratory Animals and were approved by the Nantong University Laboratory Animal Ethics Committee (approval no. IACUC20231125-1001).

Supplementary Materials

This PDF file includes:

Figs. S1 to S17
Tables S1 to S4

REFERENCES AND NOTES

1. L. Wilson, W. Stewart, K. Dams-O'Connor, R. Diaz-Arrastia, L. Horton, D. K. Menon, S. Polinder, The chronic and evolving neurological consequences of traumatic brain injury. *Lancet Neurol.* **16**, 813–825 (2017).
2. M. C. Dewan, A. Rattani, S. Gupta, R. E. Baticulon, Y. C. Hung, M. Punchak, A. Agrawal, A. O. Adeleye, M. G. Shrime, A. M. Rubiano, J. V. Rosenfeld, K. B. Park, Estimating the global incidence of traumatic brain injury. *J. Neurosurg.* **130**, 1080–1097 (2018).
3. J. V. Rosenfeld, A. I. Maas, P. Bragge, M. C. Morganti-Kossmann, G. T. Manley, R. L. Gruen, Early management of severe traumatic brain injury. *Lancet* **380**, 1088–1098 (2012).
4. E. W. Steyerberg, E. Wiegers, C. Sewalt, A. Buki, G. Citerio, V. De Keyser, A. Ercole, K. Kunzmann, L. Lanyon, F. Lecky, H. Lingsma, G. Manley, D. Nelson, W. Peul, N. Stocchetti, N. von Steinbuchel, T. Vande Vyvere, J. Verheyden, L. Wilson, A. I. R. Maas, D. K. Menon, C.-T., Case-mix, care pathways, and outcomes in patients with traumatic brain injury in CENTER-TBI: A European prospective, multicentre, longitudinal, cohort study. *Lancet Neurol.* **18**, 923–934 (2019).
5. B. Roozenbeek, A. I. Maas, D. K. Menon, Changing patterns in the epidemiology of traumatic brain injury. *Nat. Rev. Neurol.* **9**, 231–236 (2013).
6. P. Bouzat, F. X. Ageron, M. Thomas, C. Vallot, S. Hautefeuille, C. Schilte, J. F. Payen, Modeling the influence of age on neurological outcome and quality of life one year after traumatic brain injury: A prospective multi-center cohort study. *J. Neurotrauma* **36**, 2506–2512 (2019).
7. H. Dhungana, T. Malm, A. Denes, P. Valonen, S. Wojciechowski, J. Magga, E. Savchenko, N. Humphreys, R. Grencis, N. Rothwell, J. Koistinaho, Aging aggravates ischemic stroke-induced brain damage in mice with chronic peripheral infection. *Aging Cell* **12**, 842–850 (2013).

8. R. C. Knopp, S. H. Lee, M. Hollas, E. Nepomuceno, D. Gonzalez, K. Tam, D. Aamir, Y. Wang, E. Pierce, M. BenAissa, G. R. J. Thatcher, Interaction of oxidative stress and neurotrauma in ALDH2−/− mice causes significant and persistent behavioral and pro-inflammatory effects in a tractable model of mild traumatic brain injury. *Redox Biol.* **32**, 101486 (2020).
9. R. Sharma, S. R. Shultz, M. J. Robinson, A. Belli, M. L. Hibbs, T. J. O'Brien, B. D. Semple, Infections after a traumatic brain injury: The complex interplay between the immune and neurological systems. *Brain Behav. Immun.* **79**, 63–74 (2019).
10. S. X. Shi, K. Shi, Q. Liu, Brain injury instructs bone marrow cellular lineage destination to reduce neuroinflammation. *Sci. Transl. Med.* **13**, eabc7029 (2021).
11. S. Gyoneva, R. M. Ransohoff, Inflammatory reaction after traumatic brain injury: Therapeutic potential of targeting cell-cell communication by chemokines. *Trends Pharmacol. Sci.* **36**, 471–480 (2015).
12. W. Liu, W. Chen, M. Xie, C. Chen, Z. Shao, Y. Zhang, H. Zhao, Q. Song, H. Hu, X. Xing, X. Cai, X. Deng, X. Li, P. Wang, G. Liu, L. Xiong, X. Lv, Y. Zhang, Traumatic brain injury stimulates sympathetic tone-mediated bone marrow myelopoiesis to favor fracture healing. *Signal Transduct. Target. Ther.* **8**, 260 (2023).
13. W. C. Poller, J. Downey, A. A. Mooslechner, N. Khan, L. Li, C. T. Chan, C. S. McAlpine, C. Xu, F. Kahles, S. He, H. Janssen, J. E. Mindur, S. Singh, M. G. Kiss, L. Alonso-Herranz, Y. Iwamoto, R. H. Kohler, L. P. Wong, K. Chetal, S. J. Russo, R. I. Sadreyev, R. Weissleder, M. Nahrendorf, P. S. Frenette, M. Divangahi, F. K. Swirski, Brain motor and fear circuits regulate leukocytes during acute stress. *Nature* **607**, 578–584 (2022).
14. J. G. Cheong, A. Ravishankar, S. Sharma, C. N. Parkhurst, S. A. Grassmann, C. K. Wingert, P. Laurent, S. Ma, L. Paddock, I. C. Miranda, E. O. Karakaslar, D. Nehar-Belaid, A. Thibodeau, M. J. Bale, V. K. Kartha, J. K. Yee, M. Y. Mays, C. Jiang, A. W. Daman, A. Martinez de Paz, D. Ahimovic, V. Ramos, A. Lercher, E. Nielsen, S. Alvarez-Mulett, L. Zheng, A. Earl, A. Yallowitz, L. Robbins, E. LaFond, K. L. Weidman, S. Racine-Brzostek, H. S. Yang, D. R. Price, L. Leyre, A. F. Rendeiro, H. Ravichandran, J. Kim, A. C. Borczuk, C. M. Rice, R. B. Jones, E. J. Schenck, R. J. Kaner, A. Chadburn, Z. Zhao, V. Pascual, O. Elemento, R. E. Schwartz, J. D. Buenrostro, R. E. Niec, F. J. Barrat, L. Lief, J. C. Sun, D. Ucar, S. Z. Josefowicz, Epigenetic memory of coronavirus infection in innate immune cells and their progenitors. *Cell* **186**, 3882–3902.e24 (2023).
15. R. S. Carpenter, J. M. Marbourg, F. H. Brennan, K. A. Mifflin, J. C. E. Hall, R. R. Jiang, X. M. Mo, M. Karunasiri, M. H. Burke, A. M. Dorrance, P. G. Popovich, Spinal cord injury causes chronic bone marrow failure. *Nat. Commun.* **11**, 3702 (2020).
16. K. Shi, H. Li, T. Chang, W. He, Y. Kong, C. Qi, R. Li, H. Huang, Z. Zhu, P. Zheng, Z. Ruan, J. Zhou, F. D. Shi, Q. Liu, Bone marrow hematopoiesis drives multiple sclerosis progression. *Cell* **185**, 2234–2247.e17 (2022).
17. Y. H. Ho, R. Del Toro, J. Rivera-Torres, J. Rak, C. Korn, A. Garcia-Garcia, D. Macias, C. Gonzalez-Gomez, A. Del Monte, M. Wittner, A. K. Waller, H. R. Foster, C. Lopez-Otin, R. S. Johnson, C. Nerlov, C. Ghevaert, W. Vainchenker, F. Louache, V. Andres, S. Mendez-Ferrer, Remodeling of bone marrow hematopoietic stem cell niches promotes myeloid cell expansion during premature or physiological aging. *Cell Stem Cell* **25**, 407–418.e6 (2019).
18. N. D. Powell, E. K. Sloan, M. T. Bailey, J. M. Arevalo, G. E. Miller, E. Chen, M. S. Kobor, B. F. Reader, J. F. Sheridan, S. W. Cole, Social stress up-regulates inflammatory gene expression in the leukocyte transcriptome via β-adrenergic induction of myelopoiesis. *Proc. Natl. Acad. Sci. U.S.A.* **110**, 16574–16579 (2013).
19. A. A. Patel, Y. Zhang, J. N. Fullerton, L. Boelen, A. Rongvaux, A. A. Maini, V. Bigley, R. A. Flavell, D. W. Gilroy, B. Asquith, D. Macallan, S. Yona, The fate and lifespan of human monocyte subsets in steady state and systemic inflammation. *J. Exp. Med.* **214**, 1913–1923 (2017).
20. P. B. Narasimhan, P. Marcovecchio, A. A. J. Hamers, C. C. Hedrick, Nonclassical monocytes in health and disease. *Annu. Rev. Immunol.* **37**, 439–456 (2019).
21. S. J. Morrison, A. M. Wandycz, K. Akashi, A. Globerson, I. L. Weissman, The aging of hematopoietic stem cells. *Nat. Med.* **2**, 1011–1016 (1996).
22. D. J. Rossi, D. Bryder, J. M. Zahn, H. Ahlenius, R. Sonu, A. J. Wagers, I. L. Weissman, Cell intrinsic alterations underlie hematopoietic stem cell aging. *Proc. Natl. Acad. Sci. U.S.A.* **102**, 9194–9199 (2005).
23. K. Young, S. Borikar, R. Bell, L. Kuffler, V. Philip, J. J. Trowbridge, Progressive alterations in multipotent hematopoietic progenitors underlie lymphoid cell loss in aging. *J. Exp. Med.* **213**, 2259–2267 (2016).
24. D. B. McKim, W. Yin, Y. Wang, S. W. Cole, J. P. Godbout, J. F. Sheridan, Social stress mobilizes hematopoietic stem cells to establish persistent splenic myelopoiesis. *Cell Rep.* **25**, 2552–2562.e3 (2018).
25. R. H. Cho, H. B. Sieburg, C. E. Muller-Sieburg, A new mechanism for the aging of hematopoietic stem cells: Aging changes the clonal composition of the stem cell compartment but not individual stem cells. *Blood* **111**, 5553–5561 (2008).
26. C. A. Mitchell, E. V. Verovskaya, F. J. Calero-Nieto, O. C. Olson, J. W. Swann, X. Wang, A. Herault, P. V. Dellorusso, S. Y. Zhang, A. F. Svendsen, E. M. Pietras, S. T. Bakker, T. T. Ho, B. Gottgens, E. Passegue, Stromal niche inflammation mediated by IL-1 signalling is a targetable driver of haematopoietic ageing. *Nat. Cell Biol.* **25**, 30–41 (2023).
27. C. Lopez-Otin, M. A. Blasco, L. Partridge, M. Serrano, G. Kroemer, Hallmarks of aging: An expanding universe. *Cell* **186**, 243–278 (2023).
28. M. Magatti, F. Pischiutta, F. Ortolano, A. Pasotti, E. Caruso, A. Cargnoni, A. Papait, F. Capuzzi, T. Zoerle, M. Carbonara, N. Stocchetti, S. Borsa, M. Locatelli, E. Erba, D. Prati, A. R. Silini, E. R. Zanier, O. Parolini, Systemic immune response in young and elderly patients after traumatic brain injury. *Immun. Ageing* **20**, 41 (2023).
29. M. V. Russo, L. L. Latour, D. B. McGavern, Distinct myeloid cell subsets promote meningeal remodeling and vascular repair after mild traumatic brain injury. *Nat. Immunol.* **19**, 442–452 (2018).
30. M. Maryanovich, S. Takeishi, P. S. Frenette, Neural regulation of bone and bone marrow. *Cold Spring Harb. Perspect. Med.* **8**, (2018).
31. T. Heidt, H. B. Sager, G. Courties, P. Dutta, Y. Iwamoto, A. Zaltsman, C. von Zur Muhlen, C. Bode, G. L. Fricchione, J. Denninger, C. P. Lin, C. Vinegoni, P. Libby, F. K. Swirski, R. Weissleder, M. Nahrendorf, Chronic variable stress activates hematopoietic stem cells. *Nat. Med.* **20**, 754–758 (2014).
32. K. L. Chan, W. C. Poller, F. K. Swirski, S. J. Russo, Central regulation of stress-evoked peripheral immune responses. *Nat. Rev. Neurosci.* **24**, 591–604 (2023).
33. A. Denes, Z. Boldogkoi, G. Uhereczky, A. Hornyak, M. Rusvai, M. Palkovits, K. J. Kovacs, Central autonomic control of the bone marrow: Multisynaptic tract tracing by recombinant pseudorabies virus. *Neuroscience* **134**, 947–963 (2005).
34. C. Saleeba, B. Dempsey, S. Le, A. Goodchild, S. McMullan, A student's guide to neural circuit tracing. *Front. Neurosci.* **13**, 897 (2019).
35. G. Courties, F. Herisson, H. B. Sager, T. Heidt, Y. Ye, Y. Wei, Y. Sun, N. Severe, P. Dutta, J. Scharff, D. T. Scadden, R. Weissleder, F. K. Swirski, M. A. Moskowitz, M. Nahrendorf, Ischemic stroke activates hematopoietic bone marrow stem cells. *Circ. Res.* **116**, 407–417 (2015).
36. Y. X. Ye, C. Calcagno, T. Binderup, G. Courties, E. J. Keliher, G. R. Wojtkiewicz, Y. Iwamoto, J. Tang, C. Perez-Medina, V. Mani, S. Ishino, C. B. Johnbeck, U. Knigge, Z. A. Fayad, P. Libby, R. Weissleder, A. Tawakol, S. Dubey, A. P. Belanger, M. F. Di Carli, F. K. Swirski, A. Kjaer, W. J. Mulder, M. Nahrendorf, Imaging macrophage and hematopoietic progenitor proliferation in atherosclerosis. *Circ. Res.* **117**, 835–845 (2015).
37. D. Jahn, P. R. Knapstein, E. Otto, P. Kohli, J. Sevecke, F. Graef, C. Graffmann, M. Fuchs, S. Jiang, M. Rickert, C. Erdmann, J. Appelt, L. Revend, Q. Kuttner, J. Witte, A. Rahmani, G. Duda, W. Xie, A. Donat, T. Schinke, A. Ivanov, M. N. Tchouto, D. Beule, K. H. Frosch, A. Baranowsky, S. Tsitsilonis, J. Keller, Increased beta(2)-adrenergic signaling promotes fracture healing through callus neovascularization in mice. *Sci. Transl. Med.* **16**, eadk9129 (2024).
38. Y. Xiong, A. Mahmood, M. Chopp, Animal models of traumatic brain injury. *Nat. Rev. Neurosci.* **14**, 128–142 (2013).
39. J. Y. Peng, Z. X. Qi, Q. Yan, X. J. Fan, K. L. Shen, H. W. Huang, J. H. Lu, X. Q. Wang, X. X. Fang, L. Mao, J. Ni, L. Chen, Q. X. Zhuang, Ameliorating parkinsonian motor dysfunction by targeting histamine receptors in entopeduncular nucleus-thalamus circuitry. *Proc. Natl. Acad. Sci. U.S.A.* **120**, e2216247120 (2023).
40. Z. X. Qi, K. L. Shen, J. Y. Peng, X. J. Fan, H. W. Huang, J. L. Jiang, J. H. Lu, X. Q. Wang, X. X. Fang, L. Chen, Q. X. Zhuang, Histamine bidirectionally regulates the intrinsic excitability of parvalbumin-positive neurons in the lateral globus pallidus and promotes motor behaviour. *Br. J. Pharmacol.* **180**, 1379–1407 (2023).
41. J. Y. Peng, K. L. Shen, X. J. Fan, Z. X. Qi, H. W. Huang, J. L. Jiang, J. H. Lu, X. Q. Wang, X. X. Fang, W. R. Yuan, Q. X. Deng, S. Chen, L. Chen, Q. X. Zhuang, Receptor and ionic mechanism of histamine on mouse dorsolateral striatal neurons. *Mol. Neurobiol.* **60**, 183–202 (2023).
42. Q. X. Zhuang, G. Y. Li, B. Li, C. Z. Zhang, X. Y. Zhang, K. Xi, H. Z. Li, J. J. Wang, J. N. Zhu, Regularizing firing patterns of rat subthalamic neurons ameliorates parkinsonian motor deficits. *J. Clin. Invest.* **128**, 5413–5427 (2018).
43. Z. Zheng, C. Guo, M. Li, L. Yang, P. Liu, X. Zhang, Y. Liu, X. Guo, S. Cao, Y. Dong, C. Zhang, M. Chen, J. Xu, H. Hu, Y. Cui, Hypothalamus-habenula potentiation encodes chronic stress experience and drives depression onset. *Neuron* **110**, 1400–1415.e6 (2022).
44. Y. Nagai, N. Miyakawa, H. Takuwa, Y. Hori, K. Oyama, B. Ji, M. Takahashi, X. P. Huang, S. T. Slocum, J. F. DiBerto, Y. Xiong, T. Urushihata, T. Hirabayashi, A. Fujimoto, K. Mimura, J. G. English, J. Liu, K. I. Inoue, K. Kumata, C. Seki, M. Ono, M. Shimojo, M. R. Zhang, Y. Tomita, J. Nakahara, T. Suhara, M. Takada, M. Higuchi, J. Jin, B. L. Roth, T. Minamimoto, Deschloroclozapine, a potent and selective chemogenetic actuator enables rapid neuronal and behavioral modulations in mice and monkeys. *Nat. Neurosci.* **23**, 1157–1167 (2020).

Acknowledgments: We thank B. Wei and H. Wang for guidance in the study design. **Funding:** Our study was financially supported by the National Key Research and Development Program of China (2023YFC2306502 to W.S.), the National Natural Science Foundation of China (82301561 to Q.L.), the National Natural Science Foundation of China (82271415 to P.G.), the National Natural Science Foundation of China (31771143 to Q.-X.Z.), the National Natural Science Foundation of China (82322023 and 82101364 to K.S.), and the National Natural

Science Foundation of China (82371398 to W.S.). **Author contributions:** Writing—original draft: W.S., C.W., R.J., J. Shen, K.S., Z.L., Q.-X.Z. Conceptualization: W.S., C.W., K.S., and Q.-X.Z. Investigation: W.S., C.W., R.J., P.G., X.X., J. Shen, Q.L., J. Shi, X.Z., Z.L., and Q.-X.Z. Writing—review and editing: W.S., C.W., R.J., P.G., K.S., Z.L., and Q.-X.Z. Methodology: W.S., C.W., R.J., P.G., X.X., K.S., Q.L., J. Shi, X.Z., Z.L., Q.-X.Z. Resources: W.S., C.W., R.J., J. Shen, K.S., and Q.-X.Z. Funding acquisition: W.S., P.G., K.S., and Q.-X.Z. Data curation: W.S., C.W., R.J., J. Shen, K.S., Z.L., and Q.-X.Z. Validation: W.S., C.W., R.J., P.G., X.X., J. Shen, X.Z., Z.L., and Q.-X.Z. Supervision: W.S., R.J., X.J., K.S., and Q.-X.Z. Formal analysis: W.S., C.W., R.J., P.G., X.X., J. Shen, K.S., Q.L., Z.L., and Q.-X.Z. Software: W.S., C.W., R.J., P.G., X.X., J. Shen, Z.L., and Q.-X.Z. Project administration: W.S., K.S., and Q.-X.Z. Visualization: W.S., C.W., R.J., P.G., X.X., K.S., Z.L., and Q.-X.Z. All authors have read and agreed to the published version of the manuscript. **Competing interests:** The authors declare that they have no competing interests. **Data and materials availability:** All data needed to evaluate the conclusions in the paper are present in the paper and/or the Supplementary Materials.

Submitted 28 March 2024
Accepted 14 June 2024
Published 19 July 2024
10.1126/sciadv.adp5239